

Dissertation presented to the Instituto Tecnológico de Aeronáutica, in partial fulfillment of the requirements for the degree of Master of Science in the Program of Aeronautical and Mechanical Engineering, Field of Aeronautic Design, Structures and Aerospace Systems

**Jelle Jan van de Kerk**

# **A Semi-Analytical model for Mode I delamination prediction in bolted bonded composite joints**

**Dissertation approved in its final version by signatories below:**

Prof. Dr. M.V. Donadon  
Head of department of Structures  
Aeronautical and Aerospace Engineering Division  
*Advisor*

Prof. Dr. M.A. Arbelo  
Department of Structures  
Aeronautical and Aerospace Engineering Division  
*Co-Advisor*

Campo Montenegro  
São José dos Campos, SP – Brasil  
2022

## Cataloging-in Publication Data

### Documentation and Information Division

Kerk, Jelle Jan van de

A Semi-Analytical model for Mode I delamination prediction in bolted bonded composite joints/ Jelle Jan van de Kerk.

São José dos Campos, 2022

66

Dissertation of Master of Science - Course of Mechanical and Aeronautical Engineering. Area of Aeronautical Structures - Instituto Tecnológico de Aeronáutica, 2022. Advisor: Prof.Dr. Maurício Vicente Donadon. Co-advisor: Prof.Dr. Mariano Andrés Arbelo

1. Teste DCB 2. Elemento finito hierárquico 3. Método Rayleigh-Ritz 4. Mecânica da fratura 5. Simulação composta. I. Instituto Tecnológico de Aeronáutica. II. Um modelo semi-analítico para previsão de delaminação em Modo I em juntas compostas aparafusadas

## BIBLIOGRAPHIC REFERENCE

KERK, Jelle Jan van de. **A Semi-Analytical model for Mode I delamination prediction in bolted bonded composite joints.** 2022. Dissertation of Master of Science – Instituto Tecnológico de Aeronáutica, São José dos Campos

### CESSION OF RIGHTS

AUTHOR'S NAME: Jelle Jan van de Kerk

PUBLICATION TITLE: A Semi-Analytical model for Mode I delamination prediction in bolted bonded composite joints.

PUBLICATION KIND/YEAR: Dissertation / 2022

It is granted to Instituto Tecnológico de Aeronáutica permission to reproduce copies of this dissertation and to only loan or to sell copies for academic and scientific purposes. The author reserves other publication rights and no part of this dissertation can be reproduced without the authorization of the author.

---

Jelle Jan van de Kerk  
Olieslagweg, 90  
7521 JE - Enschede, Overijssel, NL  
(UT graduation number: 402)

# Acknowledgements

I wish to thank professor Mauricio Donadon and professor Mariano Arbelo for their supervision and support of this thesis. They provided helpful insights and comments throughout the time working on the project and they were willing to take up the challenge of supervising a master thesis over a long distance, during the ongoing pandemic.

Furthermore, I would like to extend my gratitude to professor Kees Venner. Firstly for selecting me for this double masters program, and secondly for his role as supervisor at the University of Twente.

I would also like to thank Giovanni Bastiani for his work and generosity in providing the experimental data used in this thesis. His results proved to really aid the understanding and improvement of the model.

My thanks goes out to the Instituto Tecnológico de Aeronáutica, the University of Twente, and everyone involved in the Double Degree Program. Although the experience was different than expected due to the pandemic, it has been a time that I will remember fondly.

Lastly I would like to personally thank my parents for their support throughout my studies. They have always been there for me and have been a helping hand in rough times.

Jelle van de Kerk

February 2022, Enschede, Netherlands

**Dedicated to Cornelis (Cees) van de Kerk**



★ 09-08-1928            -            † 16-09-2021

The first engineer in the family, in whose footsteps 2 generations of engineers follow. His support was crucial throughout my studying years, and his mental strength an inspiration. A very special grandfather.

---

# Executive Summary

The use of composite materials in aircraft has been increased over the years due to push for performance with the goal of increasing sustainability. It has also created a demand for a better understanding and better predictions of the behaviour composite structures within aircraft. Composite structures are regularly assembled using a combination of adhesive and mechanical fasteners. The objective for this research is to present a model which can accurately analyse crack growth in bolted-bonded structures which can reduce computation time compared to Finite Element Analysis (FEA).

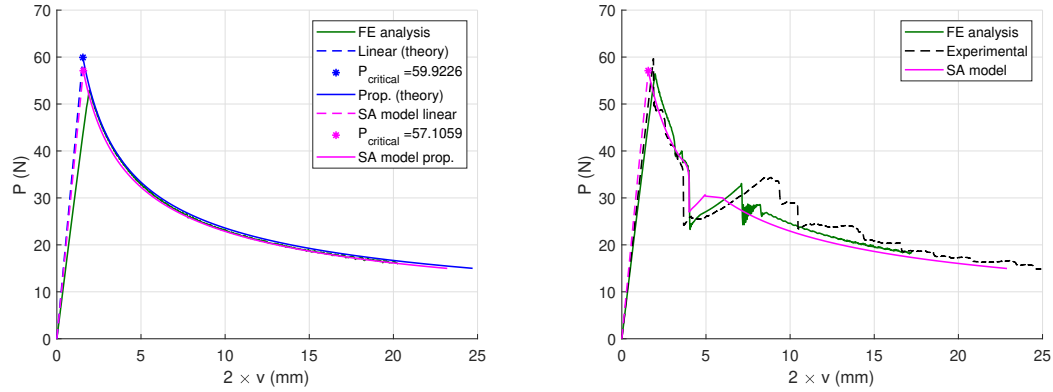
A novel Semi-Analytical (SA) model is proposed to analyse mode I delamination in bonded composite structures including fasteners used for crack arrest. The SA model uses hierarchical shape functions describe the displacement field over the Double Cantilever Beam (DCB) specimen. The specimen is divided in three domains with each a set of hierarchical shape functions to accurately describe the displacement field around the crack tip, where the central domain moves along with the crack tip.

The Principle of Minimal Potential Energy (PMPE) combined with the Rayleigh-Ritz Method are used to determine the set of equilibrium equations. The total strain energy of the virtual DCB specimen is defined in terms of the bending strain energy of the laminate, the strain energy of the bonding area between the sub-laminates modelled by an elastic foundation, and the fastener strain energy. The hole and the fastener position in the DCB specimen are accounted for in each of these terms. The overall displacement field obtained by solving the resultant set of equilibrium equations is used to define the specimen's compliance function, from which the Strain Energy Release Rate (SERR) can be determined for different load levels and crack lengths. An iterative scheme based on the Newton Raphson method is used to compute the crack lengths associated with different load levels during the delamination propagation.

A Finite Element (FE) model with Cohesive Zone Modelling (CZM) is built alongside the SA model for comparison of performance. Next to the results of the FEA, are the results of the SA model compared to experimental results, and functions derived from Bernoulli theory.

As is shown in figure 0.1a the crack growth behaviour of the SA model is identical to theoretical functions describing crack growth in a plain DCB specimen and the predictions of the FEA. The linear opening of the specimen prior to force reduction due to crack growth predicted by the theory and the SA model is stiffer than the results of the FE model. In the Bernoulli theory this is due to the assumption of a perfectly clamped base which should be elastic. The SA model is more compliant than predicted by theory but

not as compliant as the FE model.



(a) Force vs opening plot of a simple DCB specimen (b) Force vs opening plot of a DCB specimen with a hole

Figure 0.1: Performance of the SA model against theory, FE analysis, and experimental results

In figure 0.1b the performance of the SA model describing the crack growth in a DCB specimen with a hole is shown. In this graph the SA model is compared to results of the FE model and experiments. The crack growth behaviour of the SA model is indistinguishable from the other results until the hole is reached.

When the crack tip reaches the hole, the crack snaps through a certain length of the specimen until a new equilibrium is reached. This behaviour is correctly predicted by the SA model at the correct opening distance. As the crack tip leaves the hole, the SA model resumes the crack growth curve. However the FE model and the experiment both experience a curving of the crack tip front which built up tension which is released with a secondary snap through. This behaviour could not be predicted by the SA model as it is a 2 dimensional simplification which assumes a straight crack tip throughout the specimen.

The results of a DCB with an installed fastener are shown in figure 0.2. Again the crack growth behaviour of the SA model is interchangeable with the experimental and FE results. During crack arrest at the fastener the three curves experience different behaviours.

The FE model predicts behaviour that is expected if the fastener is tightened until 'finger-tight'. The fastener is loosely clamping the specimen which allows for a snap through of the crack tip through the hole. After which the crack is arrested and the opening force increases.

The SA model predicts a crack arrest which behaviour is similar to the experimental results, where the fastener in place is tightened until the nominal preload. This preload prevents the snap through behaviour of the crack tip. The crack growth is arrested in both the SA predictions as in the experimental results without a snap through.

The SA model predicts crack arrest to happen at a lower opening displacement than the experiments, which indicates that the influence of the fastener is accounted for with a smaller crack tip length in the SA model. This smaller crack tip length means the SA

model has shorter opening arms of the DCB specimen at crack arrest. This results in the stiffer opening behaviour of the SA model at crack arrest compared to the experimental results.

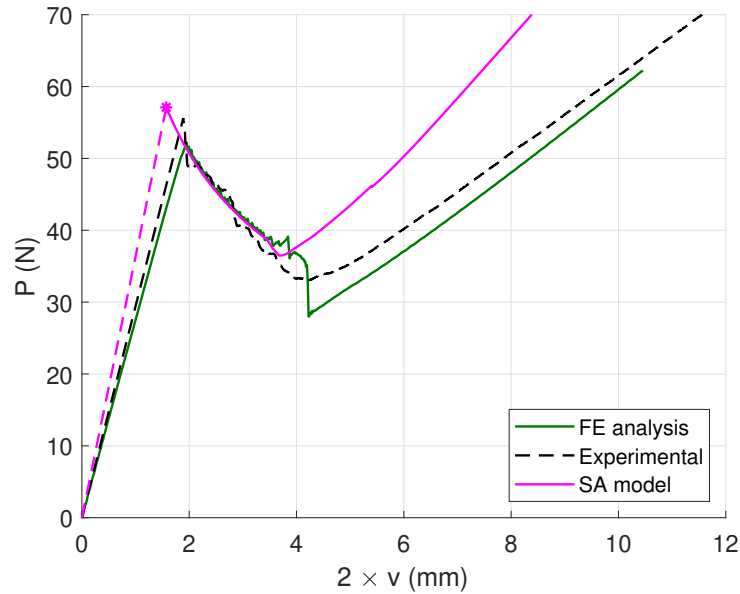


Figure 0.2: Force vs opening plot of a DCB specimen with installed fastener

Finally a small parameter optimization is performed. There are relations between the accuracy of the results of the SA model and the length of the central domain, and between the number of hierarchical shape functions used and the accuracy and run time of the model. Furthermore is the computation time, compared to FEA, reduced from hours to minutes. It is recommended to further explore the length of the central domain and its relation to the fastener diameter.

The results of the SA model in terms of load-displacement curves are compared with Cohesive Zone based nonlinear Finite Element (FE) predictions and experimental results. A very good agreement between results obtained using the SA model, the FE model and the experimental results is found. The proposed SA model allows for large parametric studies at very low computational cost, and is a powerful tool for preliminary analysis, design, and optimization of bolted-bonded composite parts. The model could help to speed up the search for higher performance part within the aviation industry.

# List of Figures

0.1	Performance of the SA model against theory, FE analysis, and experimental results . . . . .	v
0.2	Force vs opening plot of a DCB specimen with installed fastener . . . . .	vi
1.1	Examples of co-curing, co-bonding, and secondary bonding . . . . .	1
1.2	Example of joints including fasteners in aircraft . . . . .	2
2.1	Delamination modes in composite structures . . . . .	8
2.2	Illustration of composite failures on various scales . . . . .	8
2.3	Traction separation curve in the cohesive zone[6] . . . . .	10
2.4	Schematic of a beam on a Pasternak/Winkler foundation . . . . .	11
3.1	Schematic overview of a DCB test with fasteners . . . . .	12
3.2	Overview of the SA model . . . . .	14
3.3	Overview of the specimen split in domains . . . . .	16
3.4	Schematic of the DCB specimen on an elastic foundation . . . . .	18
3.5	Description of the width over the length . . . . .	25
3.6	Varying scenarios due to the multiple domains, dimensions are not to scale	25
3.7	Example of the compliance of the model as function of crack tip length. .	27
3.8	Example of the $g(a)$ function and the implementation of the NR scheme	30
4.1	Model of the plain DCB specimen . . . . .	32
4.2	Meshes refinement around the hole . . . . .	33
4.3	The pin and collar . . . . .	34
4.4	Overview of the FE model of a full DCB specimen with fastener . . . . .	35
5.1	Overview of the test specimen and its dimensions . . . . .	37
5.2	Validation of the cohesive material modelling . . . . .	40
5.3	Comparison of the FE analysis to theoretical values . . . . .	41
5.4	Plot of the SA model of a plain DCB specimen against theory . . . . .	42
5.5	Comparison of the SA model of a plain DCB specimen with theory and FEA	43
5.6	Comparison of the SA model of a DCB specimen with a hole with FEA and experimental data . . . . .	44
5.7	Plot of the crack tip front at multiple moment of the FE analysis of a DCB specimen with a hole. . . . .	46
5.8	Enlargements of regions IV, V, and VI . . . . .	46
5.9	Comparison of the SA model of a DCB specimen with a hole with multiple experiments . . . . .	48

---

5.10	Comparison of the SA model of a DCB specimen with a fastener with FEA and experimental data . . . . .	49
5.11	Comparison of experiments with fasteners loaded according to the nominal preload and finger tight . . . . .	50
5.12	Comparison of the SA model against experiments with the fasteners tightened with nominal load . . . . .	51
5.13	Crack tip front of DCB with fastener, the fastener is hidden in the images	51
5.14	Comparison of the SA model against the FE analyses . . . . .	52
5.15	Comparison of the FE model against experiments with the fasteners tightened finger tight . . . . .	53
5.16	The effect of varying length $s$ ( $m$ ) on the accuracy of the SA model . . .	53
5.17	Approximation of the crack tip front at crack arrest . . . . .	54
5.18	Comparison of crack arrest of the regular SA model . . . . .	55
5.19	Graphs of different order models plotted against an experimental curve . .	57
5.20	The influence of the length $s$ on the SA model . . . . .	58
A.1	Raw vs. filtered data of the Plain DCB FE model . . . . .	65
A.2	Raw vs. filtered data of the DCB specimen with hole FE model . . . . .	66
A.3	Raw vs. filtered data of the DCB specimen with hole and fastener FE model	66

# List of Tables

4.1	Laminate material data [34, 35] . . . . .	31
4.2	Epoxy material data [8, 9] . . . . .	33
4.3	Mechanical properties of the fastener [9] . . . . .	34
5.1	Dimensions of the specimen ( <i>mm</i> )[34] . . . . .	38
5.2	Parameters used for the Bernoulli theory . . . . .	39
5.3	Other parameters used in the SA model . . . . .	39
5.4	Results or order variation . . . . .	56
5.5	Results of <i>s</i> variation . . . . .	58

# List of Abbreviations and Symbols

## Abbreviations

CLPT	Classical Laminate Plate Theory
CZM	Cohesive Zone Modelling
DCB	Double Cantilever Beam
FE	Finite Element
FEA	Finite Element Analysis
HFEM	Hierarchical Finite Element Method
NR	Newton Raphson (method)
PMPE	Principle of Minimum Potential Energy
PTFE	Polytetrafluorethylene
SA	Semi Analytical
SERR	Strain Energy Release Rate
UD	Unidirectional
VCCT	Virtual Crack Closure Technique

## Material properties

$\rho$	Material density	$kg/m^3$
$t_{ply}$	Laminate ply thickness	$mm$
$\bar{E}_x$	Effective laminate elastic modulus material direction $x$	GPa
$\bar{G}_{xy}$	Effective laminate in plane shear modulus	GPa
$\nu_{12}$	Laminate ply in plane poisson ratio	-
$E_1$	Laminate ply elastic modulus in direction 1	GPa

$E_f$	Elastic modulus of the fastener	GPa
$G_{12}$	Laminate ply in plane shear modulus	GPa
$\sigma_I^0$	Mode I delamination onset stress	MPa
$G_c$	Critical strain energy release rate	$J/m^2$
$G_{Ic}$	Critical strain energy release rate associated with mode I delamination	$J/m^2$

### Physical Parameters

$\Gamma$	Surface area energy	$J$
$\Pi$	Potential energy	$J$
$U$	Strain energy	$J$
$U_e$	Foundation extension strain energy	$J$
$U_r$	Foundation rotation strain energy	$J$
$U_{lam}$	Laminate bending strain energy	$J$
$U_{Re}$	Fastener extension strain energy	$J$
$U_{Rr}$	Fastener rotation strain energy	$J$
$W$	Work	$J$
$A$	Area	$m^2$
$A_f$	Cross-sectional area of the fastener	$m^2$
$C(a)$	Opening compliance function depending of the crack length	$mm/N$
$G$	Strain energy release rate	$J/m^2$
$G(a)$	Strain energy release rate function	$J/m^2$
$G_I$	Strain energy release rate associated with mode I delamination	$J/m^2$
$a$	Crack length	$mm$
$a^j$	Crack length prediction at NR iteration $j$	$mm$
$a_0$	Initial crack length	$mm$
$a_i$	Crack length at cycle $i$	$mm$
$b$	Width of the specimen	$mm$
$D_f$	Fastener diameter	$mm$
$D_H$	Hole diameter	$mm$

---

$h$	Total thickness of the specimen	$mm$
$h_H$	Height of half the specimen	$mm$
$L_0$	Total length of the specimen	$mm$
$L_c$	Length of the elastic foundation	$mm$
$L_f$	Length of the fastener	$mm$
$L_n$	Distance between crack tip and fastener	$mm$
$v$	Opening displacement of specimen	$mm$
$x_f$	Fastener position	$mm$
$\delta a^i$	Crack length predictor in NR iteration $j$	$mm$
$\delta_f$	Displacement at failure	$\mu m$
$\delta_{tol}$	Tolerance set for convergence of the NR method	$\mu m$
$C$	Opening compliance	$mm/N$
$I_H$	Second moment of inertia of half the specimen thickness	$mm^4$
$k_e$	Foundation extensional stiffness factor	$N/m$
$k_r$	Foundation rotational stiffness factor	$N/m$
$k_{Re}$	Fastener extensional stiffness factor	$N/m$
$k_{Rr}$	Fastener rotational stiffness factor	$N/m$
$P$	Applied load	$N$
$P_c$	Critical load	$N$
$P_{next}$	Load for next crack grow cycle	$N$
$s$	Half the length of the second domain	$mm$
$s_1$	Location of node 1 of the second domain	$mm$

### Other Symbols

$[\mathbf{N}(\mathbf{x})]$	Vector of shape functions for the complete specimen
$[\tilde{K}]$	Total specimen stiffness matrix
$[K_B]$	Bending stiffness matrix
$[K_e]$	Foundation extension stiffness matrix
$[K_r]$	Foundation rotation stiffness matrix

- 
- $[K_{Re}]$  Fastener extension stiffness matrix
- $[K_{Rr}]$  Fastener rotation stiffness matrix
- $[N^j(x)]$  Horizontal vector of shape functions for domain  $j$
- $\alpha, \beta, \eta$  Exponential parameters for various fracture criteria
- $\kappa$  Timoshenko shear correction factor
- $\phi_i$  Shape function of order  $i$
- $\xi$  Dimensionless natural coordinate
- $\{\mathbf{c}_i\}$  Generalized Ritz coordinates vector for the complete specimen
- $\{c_i^j\}$  Generalized Ritz coordinates vector for domain  $j$
- $\{Q\}$  Generalized load vector of the specimen
- $b(x)$  Function describing the width of the specimen at the hole
- $g(a)$  SERR function built for the NR method
- $v(x)$  Vertical displacement function for the complete specimen
- $v^j(x)$  Vertical displacement function for domain  $j$

# Contents

<b>1</b>	<b>Introduction</b>	<b>1</b>
1.1	General . . . . .	1
1.2	Objective . . . . .	3
1.3	Dissertation structure . . . . .	3
<b>2</b>	<b>Literature review</b>	<b>4</b>
2.1	Previous works on the topics . . . . .	4
2.2	Theoretical foundation . . . . .	7
<b>3</b>	<b>Methodology</b>	<b>12</b>
3.1	Derivations of basic theoretical formulations . . . . .	12
3.2	Overview of the SA model . . . . .	13
3.3	Principle of Minimum Potential Energy (PMPE) . . . . .	15
3.4	Describing the displacement field and Work . . . . .	15
3.5	Elastic strain energy . . . . .	18
3.6	Total potential energy . . . . .	21
3.7	Integration of the matrices over the three domains . . . . .	23
3.8	Strain Energy Release Rate (SERR) . . . . .	26
3.9	Newton Raphson method for crack growth . . . . .	28
<b>4</b>	<b>Finite Element model</b>	<b>31</b>
4.1	Base design . . . . .	31
4.2	Implementation of the hole . . . . .	33
4.3	Implementation of the fastener . . . . .	34
4.4	Simulation settings & parameters . . . . .	35
<b>5</b>	<b>Results</b>	<b>37</b>
5.1	Specimen Details . . . . .	37
5.2	FE model validation . . . . .	40
5.3	Plain DCB . . . . .	41
5.4	DCB with a hole . . . . .	43
5.5	DCB with a fastener . . . . .	48
5.6	Improvements of the SA model . . . . .	55
<b>6</b>	<b>Conclusions</b>	<b>60</b>
	<b>References</b>	<b>62</b>

<b>Appendix</b>	<b>65</b>
<b>A Filtering of FE data</b>	<b>65</b>

# Chapter 1

## Introduction

### 1.1 General

The global drive for sustainability pushes the aviation industry to strive for higher performance aircraft to limit their global impact. This push to increase the performance of aircraft can be realized by reducing aircraft weight while increasing loads, or designing the aircraft to be able to withstand more extreme conditions. One of the important factors in the design performance is the material used.

The use of composite materials in aircraft has been increasing over the last couple of years and with it the demand to fully understand the design limitations of the material. The advantages of composites materials compared to their metallic counterparts can range from their high strength to weight ratio or their corrosion resistance to their impact resistance or thermal stability.

Not only are composite materials able to beat their counterparts in performance, they can have large advantage in fabrication. Composite materials can be formed in complex shapes which are either impossible to construct in metallic materials, or require excessive machining and material waste, or require the production and assembly of multiple sub structures. Composite material structures can be widely found in aircraft nowadays. They can be found in wings, tail vertical or horizontal stabilizers, fuselage heads and skin, spars, and ribs.

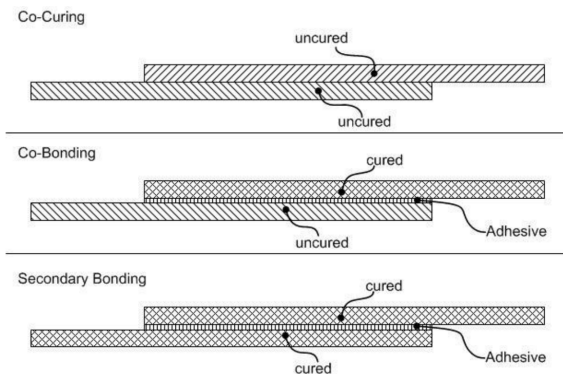


Figure 1.1: Examples of co-curing, co-bonding, and secondary bonding

However, composite structure eventually do also require assembly within aircraft. The assembly options for composite structures consist of adhesive bonding, mechanical fasteners, of a combination of both. Regular forms of adhesive bonding are co-curing and co-bonding, where at least one of the substructures still requires curing, or secondary bonding, where only the adhesive which binds the substructures requires curing.

One can ask why combinations of mechanical fasteners and adhesive bonding are used, as with careful consideration the adhesive bond can be designed to have the required strength. The problem lies within the certification of the resultant structures. Certification of operation necessary structures, such as wings, require the design to be proven by one of three techniques[1].

The design must be proof tested per designed bond, which would become unfeasibly expensive, let alone time-consuming. A second option is the design of a non-destructive test or inspection to ensure the strength of the bond over its designed lifetime. However, there has not been a method of inspection or test proven to capable in determining long term strength of such bond with non-destructive methods. Which leaves the third option, failure of the bond must be prevented by design features. This has lead to the common practice of adding mechanical fasteners to composite bonded joints.

Designs without fasteners could lead to a reduction in weight, a reduction in component thickness, and the elimination of a large part of the stress concentrations. In figure 1.2 is an example given of a part of an aircraft structure which could be designed using only adhesive bonds. However, as certification of adhesive bonds is an improbability, engineers will have to design parts with the inclusion of fasteners as mechanical prevention features, being bolted-bonded.

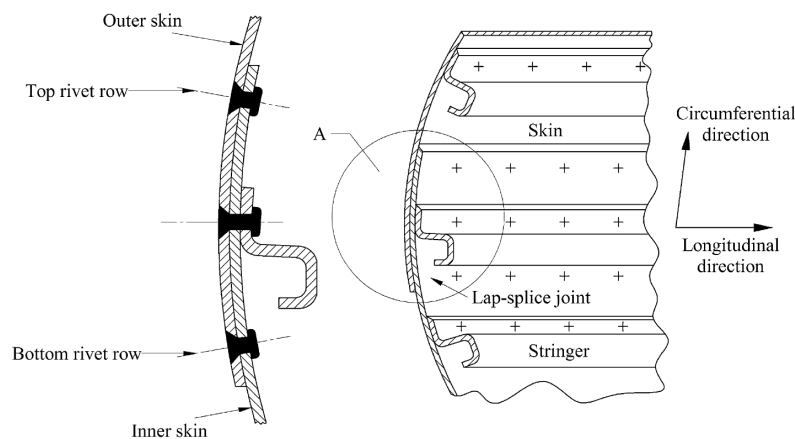


Figure 1.2: Example of joints including fasteners in aircraft

One of the most common failure modes of composite materials designers have to account for is delamination. In aircraft structures this can occur between structures which have been bonded together. The roll of mechanical fasteners for certification purposes is combined with the purpose of crack arrest, to assist in preventing delamination failure. Fasteners have been proven to provide excellent crack arrest for Mode I delamination

and acceptable crack arrest for Mode II delamination [2].

The most accurate method available at this time to predict and analyse the crack growth in composites with fasteners is the complete implementation of a specimen in a Finite Element (FE) model. However, this is a time and computational costly process, which increases time from design to production. However, as there is currently no accurate way of implementation of these fasteners in analytical crack growth models, this is the most common way to analyse crack growth in composite laminates with fasteners.

## 1.2 Objective

The objective of this study is to develop a Semi-Analytical (SA) model to derive the crack growth using the Rayleigh-Ritz Method for Double Cantilever Beam (DCB) specimens using the Strain Energy Release Rate (SERR). The crack grows when the critical SERR,  $G_c$ , is reached at the crack tip. The SA model should decrease computational time in comparison with a Finite Element Analysis (FEA) while still maintaining accurate results.

The SA model will be developed in three stages. A plain DCB specimen will be simulated, secondly the presence of a hole will be modelled, and lastly a fastener can be implemented. The results will be compared with the results of FEA and experimental data for verification of the SA model and validation of both the FE and SA model.

## 1.3 Dissertation structure

The research presented in this thesis was produced in four phases. The first phase is presented in the next chapter and consists of the literature review and theory foundation. In this phase previous works on the analysis of composites and its failure modes and mechanics are reviewed. It focuses on descriptions of composite failures using SA or numerical models, and describes the possibilities and limitations of the methods described. Afterwards is the theory discussed on which the SA and FE model will be developed.

The second phase of the research was the development of the SA and the FE model. These models were developed simultaneously next to each other in the three stages described above. The development of the SA model is described in chapter 3 and the FE model in chapter 4.

This phase was the most time-consuming step of the thesis as the models had to provide theoretically reasonable results before the implementation of the next stage could commence. It was also found in this phase that adjustments had to be made to the original hypothetical model to acquire the preferred level of performance.

The third phase was initiated when the second phase was still in its final stages. This phase was focused on analysing the stability and precision of the model. This was used to explore optimizations within the models to improve both speed and accuracy, which is mostly discussed in section 5.6.

The final phase was the analysis and discussion of the results, which includes drawing conclusions and formulating recommendations for further research. The topics of this phase are discussed in chapters 5 and 6.

## Chapter 2

# Literature review

### 2.1 Previous works on the topics

The failure modes and mechanics of composite materials and laminates has been extensively described by Daniel[3]. Failures in composites can be examined on a macro-, meso-, and microscopic scale, where failures on larger scales can be traced back to mechanics on smaller scales. All failures can eventually be described in fundamental terms on a microscopic level, including; failure of the matrix in tension, compression, or shear, failure on the matrix-fiber interface, and failure of the fiber in tension or compression. One such failure is delamination, which is dominated by failure of the matrix and failure on the matrix fiber interface. These failures are either tensile, or shear depending on the delamination mode to which the composite is subjected.

The use of fasteners as a form of crack arrest in delamination was studied by Lin et al.[2] on behalf of the FAA. The crack arrest capability of fasteners was shown for both mode I and mode II delamination. While mode I delamination is suppressed by the clamping of the fastener of the specimen, mode II delamination is eventually arrested by load transfer by friction and by shear loading of the fasteners after allowing the crack to propagate past the first fastener.

They also developed an analytical model consisting of springs based on the Principle of Minimal Potential Energy (PMPE) and the Rayleigh-Ritz method to approximate opening behaviour in mixed mode delamination for a given crack length. The model showed to be accurate in predicting the opening force of failure for various crack lengths. It must be noted that this model was created with the crack tip already located past the fastener, thus it does not show the crack being arrested.

For modelling in FE software, Liu[4] has shown that crack arrest behaviour can be modelled for both Mode I and II loading, including with multiple fasteners. He was using a two-dimensional model with the Virtual Crack Closure Technique (VCCT). Whereas in mode I the crack is fully arrested at the first fastener, in mode II the crack growth is slowed down until the crack front has passed the fasteners, similar to the results obtained by Lin et al. It was also shown that parametric studies for crack growth can be executed in FE software, for parameters of laminate stiffness, fastener stiffness, coefficient of friction, and interface toughness.

Next to the VCCT, another technique for modelling crack growth is the use of cohesive elements as a Cohesive Zone Model (CZM). Turon[5] has given an overview of the use of CZM for the analysis of delamination in composite materials. The CZM approach has been tested with multiple loading conditions; quasi-static, fatigue loading and low velocity impact. Furthermore, guidelines are established for a proper setup of a FE analysis and how to determine model parameters. The limitations of the method for the various loading conditions on specimens are discussed. A similar overview is presented by Hallet[6] but with further elaboration on the traction-displacement curves, mesh refinement, and the added complexity of mixed mode loading.

Oliveira & Donadon[7] discussed the damage prediction functions of the CZM for single and mixed mode applications. It was shown that with linear unloading and reloading behaviour, the element degradation function must also be linear to avoid energy loss in the residual strength in the element. Furthermore, various combinations of damage criteria and fracture energy criteria are compared and discussed, and their limitations noted.

The validity of FE modelling crack growth with a CZM has been further proven in Donadon & Lauda[8]. They present FE models for various delamination modes and different mixed mode ratios using explicit time integration schemes. For this they modelled DCB, edge-notched four-point bending (4ENF), mixed mode bending (MMB), and mixed mode flexure (MMF) tests using CZM. They found a good correlation between the numerical models and experimental results available in open literature.

De Melo[9] has shown that FE modelling using a CZM in three dimensions is a valid way of analysing crack growth in DCB specimens including fasteners. The study includes the use of single and double fastened specimens and is used to set up further research into the FE modelling of pure mode II specimens. The model was verified compared to theoretical values and the previously validated FE model from Donadon & Lauda[8].

Analytical models of DCB specimens mostly consist of beams connected to an elastic foundation along the specimen symmetry plane. The different uses of elastic foundations for analytical modelling has been extensively discussed by Olssen[10]. The compliance descriptions of an Euler-Bernoulli beam on a Winkler foundation by Carlsson[11] were compared to the compliances described by a Pasternak foundation by Kanninen[12], and various other models. The argument is made that Pasternak foundations in combination with an Euler-Bernoulli beam are exhibiting too stiff behaviour for unidirectional test specimens, as the shear stiffness of the non-cracked part is accounted for twice, and Olssen concludes that Winkler foundations with shear deformable Timoshenko beams should be the default basis of model development.

Carlsson[11] is using a combination of a Winkler foundation with an Euler-Bernoulli beam where he expands the analytical model to use angle ply laminates instead of only unidirectional laminates. For this he adapts the laminate homogenization method of Hyer & Knott[13]. The model predicts accurate compliance curves versus crack length for the various layups. The deviation increases with higher off-angle laminates but is

still in good agreement with experimental values.

Further discussion about correct modelling of an elastic foundation in DCB specimens is presented by Shokrieh & Rarani[14]. They present opposing views, in which they argue that a Pasternak foundation with a Timoshenko beam will give better predictions of the compliance for both unidirectional and angle ply laminates. They expand the model from Carlsson to use angle ply laminates with a Timoshenko beam and compare it to various combinations of beam models and elastic foundations. They argue that, even though their model of a Timoshenko beam on a Pasternak foundation offers slightly less accurate results for unidirectional layups, it has a higher accuracy compliance predictions with higher off-angle laminates, and thus must be used as a general case.

This leaves the aspect of describing composite behaviour using the Rayleigh Ritz approximation method. One of the studies using the Rayleigh Ritz method has been the work of Kharazi & Ovesy[15]. In their work they have described the buckling behaviour of a laminate with a through-width delamination. Their specimen was divided into multiple sublaminates. They used the Classical Laminate Plate Theory (CLPT) in combination with the Rayleigh Ritz method and simple polynomials to determine the critical buckling load. They presented a parametric study for various relations and dimensions, which were verified by FE analyses.

There have been various other works using the Rayleigh Ritz method to describe the buckling behaviour of composite structures. One of these is presented by Vescovini & Bisagni[16], where a stiffened panel is analysed for its buckling behaviour. They use the panel's symmetry to simplify its description, which results in sub-elements with large aspect ratios. Trigonometric functions are used to describe the elements where the connection between sub elements was established using superposition of functions describing simply supported and clamped boundary conditions. The stiffened panel was subjected to combined compressive and shear loads, for which they verified their results with FE analysis.

The division of a larger specimen in sub panels has also been used by Castro & Donadon[17], where the buckling and vibrational behaviour of a T-stiffened panel has been described. They have used a penalty approach to connect the different sub panels in their assembly. In this method they propose to calculate the penalty stiffnesses based on the properties of the sub-laminates connected to prevent numerical instability. As the same set of hierarchical polynomial functions has been used for all sub panels, the analytical integration of the displacement functions was possible in combination with look-up tables for efficient integration. They conclude their work by comparing their results for buckling lodes for various modes and their respective shape with FE analysis, which have a very good agreement.

An alternative for the penalty method to assemble sub elements in the Rayleigh Ritz method has been used by Da Silva et al.[18] to predict buckling in stiffened panels in pure shear loading. Their model was developed to include bonding defects between panel and stiffener, with variation in defect size. In their work they present a method of matrix

condensation for the Rayleigh Ritz method, similar to matrix condensation common in FE theory. Using the same polynomial shape functions from Bardell[19] as used by Castro & Donadon[17], their model has shown to be accurate in predicting the buckling modes and the corresponding critical load. The results were compared to results of both FE analyses and experiments.

Buckling is not the only property studied using the Rayleigh Ritz method. Castro et al.[20] have used the method as a way to study the harmonic behaviour of stiffened panels excited by external forces, in this case the aeroelasticity of the panel in supersonic flow. Their specimen was divided between the panel and the stiffener. They use Classical Laminate Theory (CLT) to describe the elastic strains, which allows them to account for different lay-ups in the stiffener and panel, and thus perform a parametric study. Castro et al. have shown to be accurate compared to several numerical results which are available in open literature, in both vibration mode and frequency.

The work of Castro et al.[20] was expanded by De Matos et al.[21]. Their work attempts to implement material property change dependent on temperature, allowing for a temperature dependence in the results of the Rayleigh Ritz method. They are using a micromechanical formulation of the laminate which accounts for material phase transformation in combination with CLPT to formulate the relation between property and temperature. After they confirm the predictions of the model with different FE analysis in the literature, a parametric study for varying configurations, lay-ups and material placement was performed. The hierarchical functions in the model showed the ease of improving accuracy without changing sub element sizes as is common in FE approaches.

## 2.2 Theoretical foundation

As stated earlier, delamination is the most common form of failure within composite structures. It occurs between layers of the laminate and can occur due to three different loading modes or any combination of these three.

The first mode is peeling mode, which results in a pure bending in the arms and a transverse load at the crack tip. This is often the weakest form of laminates as they often have no fibers in a transverse direction through the fiber or fabric layers to resist the transverse forces applied.

The second mode is a plain shearing mode. These loads can be taken better by composite structures as they have fibers running in the loading direction.

The third mode is a scissoring shearing mode. These loads are a combination of shear and moments. Thus, a combination a various fiber orientation can help the composite in resisting these loads.

A schematic overview of these delamination modes can be seen in figure 2.1. For this thesis, only mode I loading will be taken into consideration.

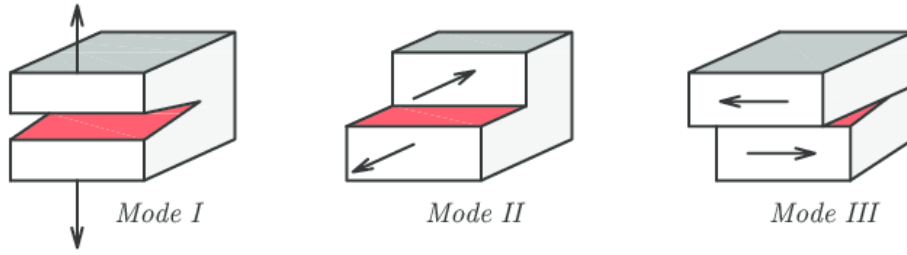


Figure 2.1: Delamination modes in composite structures

On a microscopic scale, the failure of composite materials can be described by a number of failure mechanisms. These are tensile, compressive, or shear failure of the matrix material, fiber-matrix debonding, fiber fracture, and fiber buckling. For delamination in mode I, fiber-matrix debonding and tensile failure of the matrix material are the dominant mechanics[22, 3]. An important part in the failure mechanics is the stress concentration in the matrix material around this fiber-matrix interface caused by the fiber.

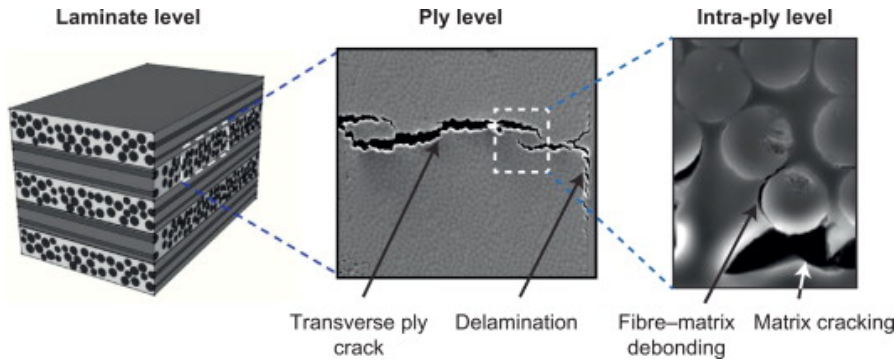


Figure 2.2: Illustration of composite failures on various scales

A standard procedure to analyse crack propagation is to look at the energy balance as done by Griffith[23]. Crack growth is an increase in surface area,  $A$ , which requires an increase in surface area energy  $\Gamma$ . The total potential energy of a system,  $\Pi$ , is the elastic strain energy minus the surface energy. Thus in order for the crack to grow, the total potential energy of the system decreases.

$$\frac{\partial \Pi}{\partial A} = \frac{\partial U}{\partial A} - \frac{\partial \Gamma}{\partial A} \quad (2.1)$$

Irwin[24] further developed this method to derive the Strain Energy Release Rate (SERR), also given by  $G$ , see equation (2.2). The SERR is the loss of potential energy per unit area of crack growth. Using the additional assumption that during brittle fracture the energy dissipation zone's shape and size stays constant, he derived that the energy change per unit area is a material constant. This material constant is the critical energy release rate and can be written as  $G_c$

$$G = -\frac{\partial \Pi}{\partial A} \quad (2.2)$$

This critical SERR can be split for the various delamination modes of a composite structure,  $G_{Ic}$ ,  $G_{IIc}$ , and  $G_{IIIc}$  for mode I, II, and III respectively. The values for mode I and II can be determined by ASTM standardized tests, using the DCB test for mode I or the ENF test for mode II. Even though there have been multiple proposals for mode III delamination test, there has not been a standardized form established yet. A common feature with these proposals is that the proposed test are not able to completely eliminate contribution of mode II delamination.

To combine these critical SERRs for various loading scenarios and determine if crack growth or fracture is occurring, there have been multiple fracture criteria proposed and used[25]. One of these is the simple Power Law function proposed by Reeder[26] as given in equation (4.2).

$$\left(\frac{G_I}{G_{Ic}}\right)^\alpha + \left(\frac{G_{II}}{G_{IIc}}\right)^\beta = 1 \quad (2.3)$$

The parameters  $\alpha$  and  $\beta$  must be determined using experimental data for various mode mixities. For the special case of  $\alpha = 1 = \beta$  the criterion becomes linear between  $G_{Ic}$  and  $G_{IIc}$ .

Another common failure criterion, often used in 2D modelling, is the BK criterion proposed by Benzeggagh & Kenane[27], which is given in equation (2.4). This criterion only needs one parameter  $\eta$  to be fitted to experimental data.

$$G_c = G_{Ic} + (G_{IIc} - G_{Ic}) \left(\frac{G_{II}}{G_T}\right)^\eta \quad (2.4)$$

CZM uses the concept of a zone of material degradation ahead of the crack tip. This concept was first conceived by Dugdale[28], closely followed by Barenblatt[29]. The method uses the assumption that material will behave linear elastically under the remaining traction forces until the interface tensile strength,  $\sigma_{max}$ . If the material is strained beyond the tensile stress, its ability to dissipate the strain energy caused by deformation will degrade.

There are various forms of degradation functions that can be used, e.g. exponential, trapezoidal, or perfectly plastic. In figure 2.3 the linear degradation is shown in a traction separation curve, as this is the most used degradation slope and the simplest to use in numerical calculations. In the CZM, the energy absorbed by the material, which is the area under the curve, must be equal to  $G_{Ic}$  when the material is fully degraded at the displacement  $\delta_f$ . If the material is fully degraded, it can no longer bear any stresses and is therefore 'released', meaning the crack has grown.

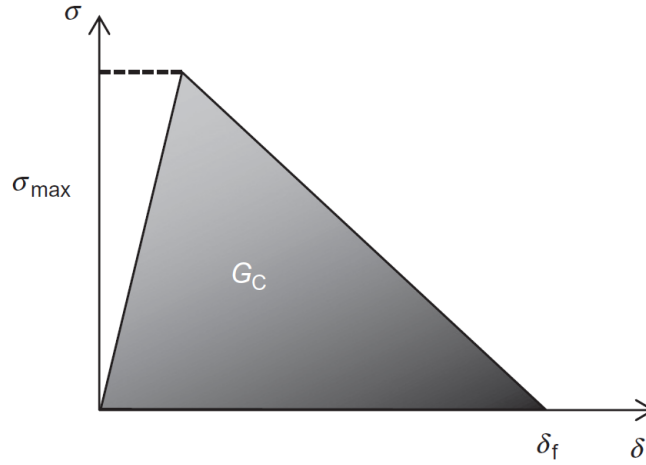


Figure 2.3: Traction separation curve in the cohesive zone[6]

The SA model presented in this thesis will build on work from Rayleigh & Ritz[30], and Bardell[19]. Bardell was active in research in the Hierarchical Finite Element Method (HFEM). HFEM is mostly used to study vibrations in plates and other structures. The method is based on increasing the interpolation functions between nodes of the elements, either increasing accuracy of the FE analysis, or reducing the number of elements needed for the analysis, or both.

The first 4 interpolation functions are the same cubic polynomials as in ordinary FE analysis. The higher order functions are calculated using equation (2.5), which is an adaptation of Legendre polynomials by Rodrigues[31].

In this formula  $\xi$  is the dimensionless internal elemental coordinate, or natural coordinate, which runs from -1 to 1. Within the formula there is a double factorial,  $n!!$ , as well. This double factorial must be interpreted as  $n!! = n \cdot (n - 2) \cdot (n - 4) \dots (2 \text{ or } 1)$ , with special values  $0!! = (-1)!! = 1$ . The factor  $r/2$  must be taken as the integer part.

These higher order functions allow for more polynomial approximations within the element, without having value for displacement or rotation in the end nodes of the element. This means every function derived with equation (2.5) will be  $\phi_r(\xi) = 0$  and  $\frac{\partial}{\partial x} \phi_r(\xi) = 0$  in the endpoints  $\xi = -1$  and  $\xi = 1$ . This has the result that the rotation and displacement in the endpoints is only determined by the first four functions in the set, regardless of the order of functions.

$$\phi_r(\xi) = \sum_{n=0}^{r/2} \frac{(-1)^n (2r - 2n - 7)!!}{2^n n! (r - 2n - 1)!} (\xi)^{r-2n-1}, \quad r > 4 \quad (2.5)$$

The SA model will use these shape functions to model the displacement field within the DCB specimen, which requires the DCB specimen to be simplified. As stated earlier there is discussion in the researching community about the use of either a Winkler or a Pasternak elastic foundation in analytical modelling. In figure 2.4 a schematic is given of a DCB specimen on an elastic foundation. The elastic foundation is used to simulate half of the adhesive and its properties from the symmetry plane. To use only the Winkler type foundation, one would only use the vertical stiffness  $k_e$ . A Pasternak type foundation

would also account for the shear or rotational stiffness of the base,  $k_r$ . As stated earlier it is argued by Shokrieh[14] that a Timoshenko beam on a Pasternak foundation should account best for general cases.

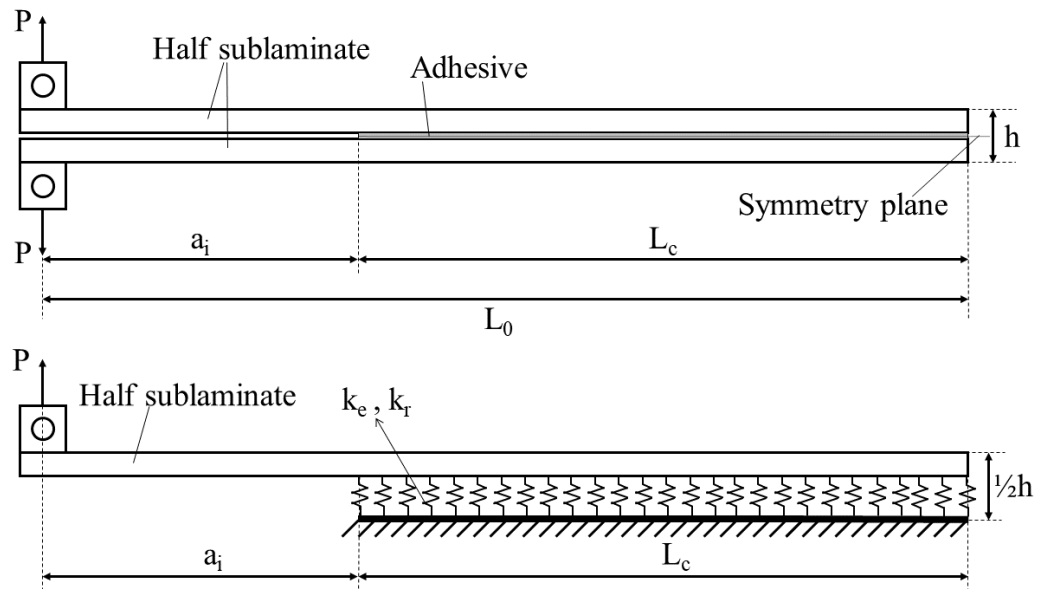


Figure 2.4: Schematic of a beam on a Pasternak/Winkler foundation

# Chapter 3

## Methodology

The analytical model will be developed around the DCB test in 2D, of which in figure 3.1 a schematic overview is given for the setup with fasteners. The model will be implemented into MatLab, version R2019b.

### 3.1 Derivations of basic theoretical formulations

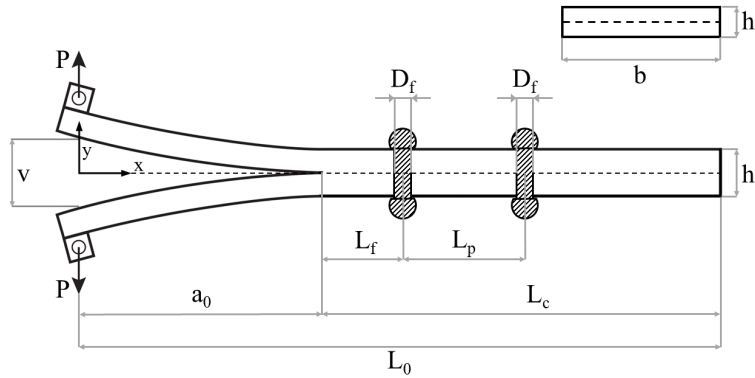


Figure 3.1: Schematic overview of a DCB test with fasteners

First, a theoretical analysis of a DCB specimen without fasteners must be made. Using the Bernoulli beam equations and the symmetry about the crack plane, the opening displacement at the beam tip can be described using force  $P$ , crack length  $a$ , elastic modulus  $E$ , and the second moment of inertia of the opening arm  $I_H$ , using half the specimen thickness.

$$v = \frac{2Pa^3}{3EI_H} \quad (3.1)$$

To find an analytical solution for the opening displacement in relation to the force during crack growth, the procedure used by Donadon[8] for a two-dimensional approach can be

followed. The opening compliance, in which the opening displacement is related to the force, can be written using Bernoulli's beam equations, equation (3.2).

$$C = \frac{v}{P} = \frac{2a^3}{3EI_H} \quad (3.2)$$

The mode I SERR can be determined using the compliance method. The strain energy in the system is equal to equation (3.3). This can be rewritten using the relation between the opening and compliance. The derivative can be taken with respect to the area for the SERR. Reducing with the assumption of a constant width  $B$  to a two-dimensional formula results in the SERR given in equation (3.4).

$$\begin{aligned} \Pi &= \frac{1}{2}Pv = \frac{1}{2}P^2C \\ \frac{\partial \Pi}{\partial A} &= \frac{P^2}{2} \frac{\partial C}{\partial A} \end{aligned} \quad (3.3)$$

$$G_I = \frac{P^2}{2B} \frac{\partial C}{\partial a} = \frac{P^2 a^2}{BEI_H} \quad (3.4)$$

When equation (3.4) is rewritten to isolate to the crack length  $a$ , it can be substituted in equation (3.1). If the critical  $G_{Ic}$  is used instead of  $G_c$  when substituting, one obtains equation (3.6). This formulation can be used to determine the opening displacement as the critical energy release rate is reached, or at crack growth.

$$a = \frac{\sqrt{G_I BEI_H}}{P} \quad (3.5)$$

$$v = \frac{2}{3} \frac{(G_{Ic} BEI_H)^{3/2}}{P^2 EI_H} \quad (3.6)$$

This small theoretical analysis of a DCB specimen without fasteners will later be used to analyse and compare the SA model to. It will be referred to as theory, or Bernoulli theory from now on.

## 3.2 Overview of the SA model

The explanation of the method of the SA model can become unclear by the amount of information given. Therefore a brief walkthrough of the workflow of the SA model will be given, broad explanations of the topics will be given in the respective sections. An overview of the model is given in figure 3.2.

The model starts with the dimensions of the DCB specimen and its features that will be analysed. These dimensions will be used to determine shape functions that will eventually describe the vertical displacement field of the specimen. However the Rayleigh Ritz coefficients for these shape functions are unknown.

The coefficients can be determined by solving a system of equations that is set up using the PMPE. The strain energy and the work in the PMPE are described using the shape functions, which can be rewritten into a system of equations. The coefficients can be substituted back in the shape functions to create a function which describes the displacement field.

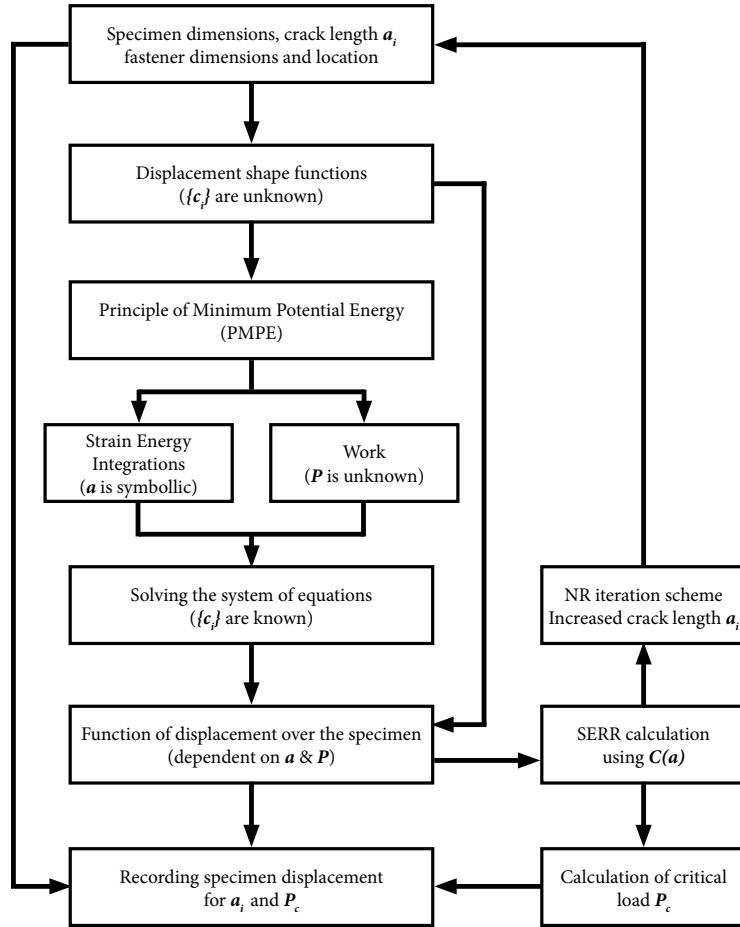


Figure 3.2: Overview of the SA model

It is important to note that the crack length is integrated symbolically. The resulting displacement function is dependent on  $a$  and  $P$ . The SERR calculation is done using the compliance method as per equation (3.4). Thus dividing the resulting displacement function by  $P$  will give the compliance function  $C(a)$ , which must be dependent on  $a$  to calculate the SERR, or the derivative would be zero.

The difference between this approach and the approach in section 3.1 is that the presence of holes and fasteners can be accounted for in the setup of the PMPE. The presence of a fastener will add terms in the strain energy equations. A hole will alter the strain energy in the laminate. Thus, the compliance function accounts for holes and fasteners.

The SERR calculation can be used to determine the critical load for a certain crack length. This critical load can then be used to determine the specimen displacement field, which can be recorded.

Lastly a Newton Raphson iteration scheme can be used to determine the crack growth for a change in loading force. The increased crack length will be used to adjust the specimen dimensions, from which the cycle starts again. The cycle can be stopped if a criterion is reached. This could be a maximum or minimum load, crack length, opening displacement, or number of cycles.

### 3.3 Principle of Minimum Potential Energy (PMPE)

The analysis will be based on the fact that during normal opening of the specimen will be in equilibrium. This static equilibrium is only breached when the crack grows, at which point the force drops until a new equilibrium is reached for the opening. The PMPE states that the system will be in equilibrium if there is no change in potential energy, therefore, the variation of the potential energy is zero.

The total potential energy of the system can be described as the elastic strain of the material, minus the work done by the forces acting on the system. The work that will be done on the system can be easily described as the opening force times the opening displacement, however this displacement is the unknown.

$$\begin{aligned}\Pi_{\mathbf{p}} &= U - W \\ \delta\Pi_{\mathbf{p}} &= 0\end{aligned}\tag{3.7}$$

### 3.4 Describing the displacement field and Work

The opening displacement is just one node of the displacement field over the DCB specimen. The vertical displacement field of the specimen will be described using its symmetry. The specimen is split in half along the bonded interface and the field only describes the vertical displacement from the symmetry plane.

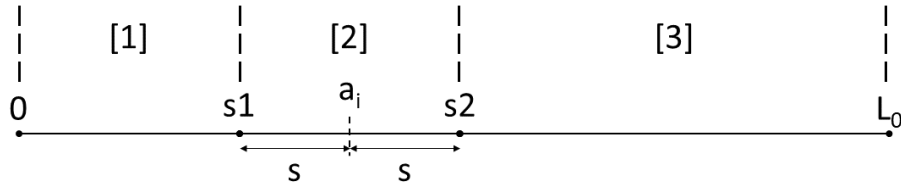
The hierarchical polynomial shape functions of Bardell[19] are used to describe the displacement field. The shape functions are multiplied with a Rayleigh-Ritz coefficient,  $c_i$ , and summed to form a function to describe the field, as given in equation (3.8). These functions together form a set of shape functions.

$$v(x) = \sum_{i=1}^n \phi_i(x)c_i\tag{3.8}$$

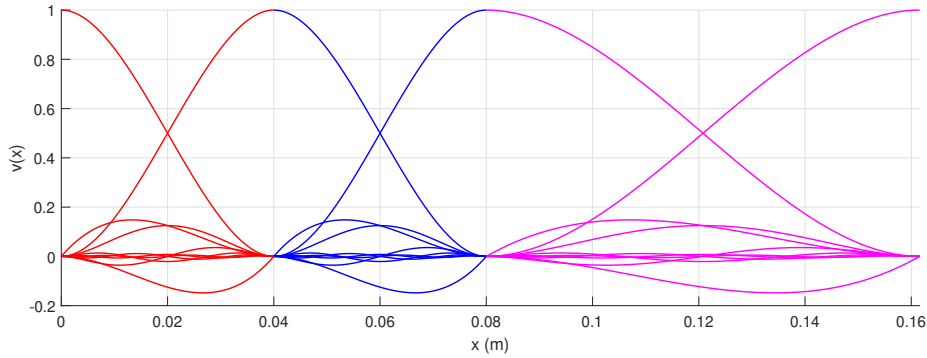
The first ten orders of functions are given in equation (3.9), where  $\xi$  is the non-dimensional elemental length running from -1 to 1. If  $x$  of the element starts at zero,  $\xi$  is related to  $x$  by  $\xi = (2x/L - 1)$ , where  $L$  is the length of the element. Further higher order functions can be determined using equation (2.5) given in section 2.2.

Initial attempts were made to describe the specimen with one set of shape functions, with ten shape functions in the set. However, those attempts did not reach the desired accuracy. Further attempts were taken to increase the order of the shape functions, but this resulted mostly in increased running times without providing the needed accuracy. Thus, the model was expanded by splitting the specimen in three domains, with each a set of shape functions. This is shown in figure 3.3. It was found that the sudden displacement change at the crack tip could not be simulated with one set of functions. The position of the middle domain is therefore linked to the position of the crack tip  $a_i$ . The distance  $s$  can be chosen to increase or decrease the size of the middle domain, which runs from  $s_1 = a_i - s$  to  $s_2 = a_i + s$ . So, the middle or second domain will move position every time the crack grows.

$$\begin{aligned}
\phi_1(\xi) &= \frac{1}{2} - \frac{3}{4}\xi + \frac{1}{4}\xi^3 \\
\phi_2(\xi) &= \frac{1}{8} - \frac{1}{8}\xi - \frac{1}{8}\xi^2 + \frac{1}{8}\xi^3 \\
\phi_3(\xi) &= \frac{1}{2} + \frac{3}{4}\xi - \frac{1}{4}\xi^3 \\
\phi_4(\xi) &= -\frac{1}{8} - \frac{1}{8}\xi + \frac{1}{8}\xi^2 + \frac{1}{8}\xi^3 \\
\phi_5(\xi) &= \frac{1}{8} - \frac{1}{4}\xi^2 + \frac{1}{8}\xi^4 \\
\phi_6(\xi) &= \frac{1}{8}\xi - \frac{1}{4}\xi^3 + \frac{1}{8}\xi^5 \\
\phi_7(\xi) &= -\frac{1}{48} + \frac{1}{16}\xi^2 - \frac{5}{16}\xi^4 + \frac{7}{48}\xi^6 \\
\phi_8(\xi) &= -\frac{3}{48}\xi + \frac{5}{16}\xi^3 - \frac{7}{16}\xi^5 + \frac{9}{48}\xi^7 \\
\phi_9(\xi) &= \frac{3}{384} - \frac{15}{96}\xi^2 + \frac{35}{64}\xi^4 - \frac{63}{96}\xi^6 + \frac{99}{384}\xi^8 \\
\phi_{10}(\xi) &= \frac{15}{384}\xi - \frac{35}{96}\xi^3 + \frac{63}{64}\xi^5 - \frac{99}{96}\xi^7 + \frac{143}{384}\xi^9
\end{aligned} \tag{3.9}$$



(a) Overview of the 3 domains the specimen is divided into



(b) Example of the sets of shape functions in the domains

Figure 3.3: Overview of the specimen split in domains

This results in the fact that the displacement field of the DCB specimen is also described in 3 domains. For each domain  $j = 1, 2, 3$ , the displacement function can be written as equation (3.10) using the shape functions and coefficients  $\{c_i^j\}$ . When the derivative is

taken from these functions, one obtains equation (3.11).

$$v^j(x) = \sum_{i=1}^n \phi_i^j(x) c_i^j = [N^j(x)] \{c_i^j\} \quad (3.10)$$

$$\begin{aligned} \frac{dv^j}{dx} &= [N_{,x}^j(x)] \{c_i^j\} \\ \frac{d^2v^j}{dx^2} &= [N_{,xx}^j(x)] \{c_i^j\} \end{aligned} \quad (3.11)$$

The shape functions of Bardell can be divided into two groups. The first four order functions,  $\phi_1$  to  $\phi_4$ , are regular cubic interpolation polynomials to describe the displacement and rotation in the ends of a domain. The higher order functions are internal displacement functions with zero displacement and rotation in the ends. For ease of handling later, the third and fourth function of the domain shape function set  $[N^j(x)]$ , which describe the displacement and rotation of the right end of the domain respectively, are moved to the end of the set.

As can be seen in figure 3.3b, the displacements in the points  $s_1$  and  $s_2$  are equal to each other using the shape functions from both domains. However, there is a difference in the rotation described by the different domain shape functions for the common point. This will result in a kink of the angle in the total displacement function  $v(x)$ . Therefore, the rotation described by each function set is evaluated in the common point. By dividing one rotation by the other, a rotation factor is made. This factor can then be applied to the rotation functions of the latter set, which alters its description of the rotation in the node to equal the rotation described by the first set. This ensures a equal description of angle by both sets of displacement functions in the common node.

$$v(x) = [[N^1(x)][N^2(x)][N^3(x)]] \left\{ \begin{array}{l} \{c_i^1\} \\ \{c_i^2\} \\ \{c_i^3\} \end{array} \right\} \quad (3.12)$$

$$v(x) = [\mathbf{N}(\mathbf{x})] \{\mathbf{c}_i\}$$

$$\begin{aligned} \frac{dv}{dx} &= [\mathbf{N}_{,x}(\mathbf{x})] \{\mathbf{c}_i\} \\ \frac{d^2v}{dx^2} &= [\mathbf{N}_{,xx}(\mathbf{x})] \{\mathbf{c}_i\} \end{aligned} \quad (3.13)$$

If these domains are combined, the total displacement function of the full specimen can be described as equation (3.12). It must be noted that the functions of  $[N^j(x)]$  are zero for values of  $x$  which do not lie within its domain. The derivatives are taken in a similar fashion and can be given by equation (3.13). The work done on the system are the forces multiplied by the displacement, as given by equation (3.14).

$$W = P \cdot v(x_P) \quad (3.14)$$

$$W = P \cdot [\mathbf{N}(\mathbf{x}_P)] \{\mathbf{c}_i\} \quad (3.15)$$

### 3.5 Elastic strain energy

The elastic strain energy of the system comes from 3 parts, the bending of the laminate, the adhesive layer, and the fastener. Elastic energy from bending can be written as equation (3.16), where  $\bar{E}_x$  is the effective sublaminde elastic modulus in x direction and  $I_H$  is the inertia of the arm, which is half of the total specimen thickness. This integral runs over the full length of the specimen.

$$U_{lam.} = \frac{1}{2} \int_0^{L_0} \bar{E}_x I_H \left( \frac{d^2 v}{dx^2} \right)^2 dx \quad (3.16)$$

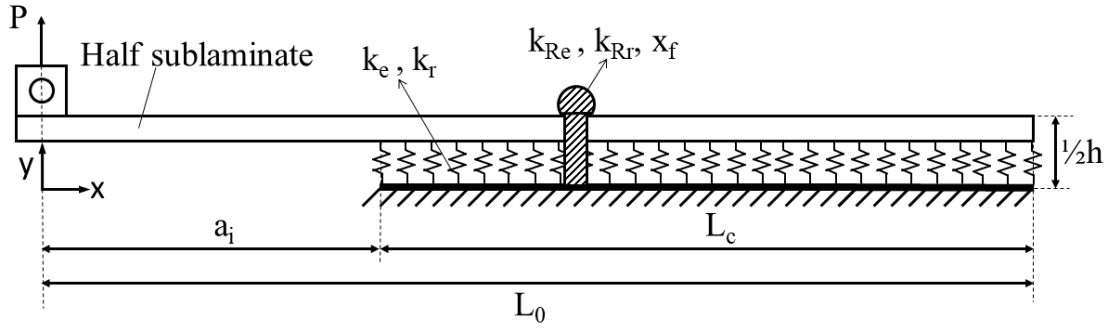


Figure 3.4: Schematic of the DCB specimen on an elastic foundation

$$\begin{aligned} k_e &= \frac{2\bar{E}_y b}{h_H} \\ k_r &= \kappa \frac{h_H \bar{G}_{xy} b}{2} \end{aligned} \quad (3.17)$$

The elastic energy from the adhesive layer can be modelled as a beam on an elastic foundation as shown in figure 3.4. The foundation has a stiffness for both extension and rotation,  $k_e$  and  $k_r$  respectively. The values for these stiffnesses are determined as described by Carlsson[11] and Shokrieh[14], using equation (3.17).

These stiffnesses are also using  $h_H$ , which is the thickness of half the specimen with half the thickness of the adhesive layer. The value  $\kappa$  is the Timoshenko shear correction factor, which for rectangular cross sections is given as  $\kappa = 5/6$ . The values are stiffnesses per unit length of the adhesive layer.

These stiffnesses also use the effective moduli of half the laminate,  $\bar{E}_y$  and  $\bar{G}_{xy}$  instead of using the properties of the adhesive, as the stresses at the interface are distributed over the height of half the specimen. These effective moduli can be determined using the laminate homogenization method from Hyer and Knott[13].

The method is an extension on classical laminate theory to account for transverse effects and it must not be forgotten to include the stiffnesses of half of the adhesive thickness. The adhesive should be seen as another ply added to the sublaminde.

$$\begin{bmatrix} C_{11} & C_{12} & C_{13} & 0 & 0 & 0 \\ C_{12} & C_{22} & C_{23} & 0 & 0 & 0 \\ C_{13} & C_{23} & C_{33} & 0 & 0 & 0 \\ 0 & 0 & 0 & C_{44} & 0 & 0 \\ 0 & 0 & 0 & 0 & C_{55} & 0 \\ 0 & 0 & 0 & 0 & 0 & C_{66} \end{bmatrix} \rightarrow \begin{bmatrix} C_{11} & C_{12} & 0 & 0 & 0 & C_{13} \\ C_{12} & C_{22} & 0 & 0 & 0 & C_{23} \\ 0 & 0 & C_{66} & 0 & 0 & 0 \\ 0 & 0 & 0 & C_{44} & 0 & 0 \\ 0 & 0 & 0 & 0 & C_{55} & 0 \\ C_{13} & C_{23} & 0 & 0 & 0 & C_{33} \end{bmatrix} \quad (3.18)$$

The 3 dimensional ply stiffness matrix is rearranged as shown above in equation (3.18), with its components defined as in classical laminate theory. During rearranging partial matrix  $[C_3]$  is defined as:

$$[C_3] = \begin{bmatrix} C_{44} & 0 & 0 \\ 0 & C_{55} & 0 \\ 0 & 0 & C_{33} \end{bmatrix} \quad (3.19)$$

The 3 dimensional transformation matrix must be rearranged as well, resulting in:

$$[T] = \begin{bmatrix} c^2 & s^2 & -2cs & 0 & 0 & 0 \\ s^2 & c^2 & 2cs & 0 & 0 & 0 \\ cs & -cs & c^2 - s^2 & 0 & 0 & 0 \\ 0 & 0 & 0 & c & s & 0 \\ 0 & 0 & 0 & -s & c & 0 \\ 0 & 0 & 0 & 0 & 0 & 1 \end{bmatrix} = \begin{bmatrix} [T_1] & [0] \\ [0] & [T_2] \end{bmatrix} \quad (3.20)$$

Using these rearranged matrices the 3 dimensional laminate matrices can be determined by integration through the thickness. The ABD matrix of the laminate is expanded to provide out of plane properties with the  $[F]$  matrix.

$$\begin{Bmatrix} \{N\} \\ \{M\} \\ \{Q\} \end{Bmatrix} = \begin{bmatrix} [A] & [B] & [0] \\ [B] & [D] & [0] \\ [0] & [0] & [F] \end{bmatrix} \begin{Bmatrix} \{\varepsilon_0\} \\ \{k\} \\ \{\varepsilon^2\} \end{Bmatrix} \quad (3.21)$$

In these expanded matrices, the  $[F]$  matrix can be found as

$$[F] = \int_{-h_H/2}^{h_H/2} [T_2] [C_3]^T [T_2]^T dz = \int_{-h_H/2}^{h_H/2} [\bar{C}_3] dz \quad (3.22)$$

The effective in plane laminate stiffnesses can be found using the ABD matrices.

$$\begin{bmatrix} [a] & [b] \\ [b] & [d] \end{bmatrix} = \begin{bmatrix} [A] & [B] \\ [B] & [D] \end{bmatrix}^{-1} \quad (3.23)$$

$$\bar{E}_x = \frac{1}{a_{11} \cdot h_H}$$

Then from  $[F]$  the effective out of plane laminate properties can be extracted using:

$$\{Q\} = [F] \{\varepsilon^2\} \rightarrow \frac{1}{h_H} \{Q\} = \frac{1}{h_H} [F] \{\varepsilon^2\} \quad (3.24)$$

$$\begin{aligned}\bar{E}_z &= \frac{F_{33}}{h_H} \\ \bar{G}_{xz} &= \frac{F_{22}}{h_H}\end{aligned}\tag{3.25}$$

These stiffnesses can then be used to determine the energy stored in the adhesive layer using the displacement function and its derivative for the extension and the rotation respectively. It is important to note that the integral runs from  $a$  to  $L_0$ , where  $a$  remains a symbolic parameter.

$$\begin{aligned}U_e &= \frac{1}{2} \int_a^{L_0} k_e (v(x))^2 dx \\ U_r &= \frac{1}{2} \int_a^{L_0} k_r \left( \frac{dv}{dx} \right)^2 dx\end{aligned}\tag{3.26}$$

The elastic energy stored in the fastener can be divided in two energies. The extension and the bending of the rivet. The bending of the rivet is perpendicular to the bending of the laminate and therefore the location at which the bending is evaluated is important. At the plane of symmetry the rotation of the fastener should be zero. However, at the end of the fastener the rotation should be equal to the rotation of the laminate. This rotation at the end of the fastener accounts for the bending strain the fastener experiences over its length throughout the thickness of the sublaminates.

The extension stiffness is a general extension stiffness formulation, indicated by  $k_{Re}$  in equation (3.29). Both stiffnesses are divided by the fastener diameter to create a stiffness per unit length in the x direction. This is needed as the strain energy is calculated using an integral in x direction.

The rotation of the rivet accounts for the bending the rivet experiences due to the opening. The rotational stiffness can be determined by seeing the fastener as free beam with moments applied to its ends. The rotation at the end is of interest as this is decided by the rotation of the laminate. The slope, or the angle, at the end can be given by a standard beam bending equation, equation (3.27).

$$\theta = \frac{ML}{2EI}\tag{3.27}$$

$$k_\theta = \frac{M}{\theta}\tag{3.28}$$

To determine a rotational stiffness, the moment per angle must be taken. The equation for the angle can be rewritten to isolate the moment  $M$ , and substituted into equation (3.28). This stiffness can be divided by the fastener diameter, similar to the extension stiffness, to obtain the rotational stiffness per length in x direction, as shown by  $k_{Rr}$  in equation (3.29).

$$\begin{aligned}k_{Re} &= \frac{2E_f A_f}{L_f D_f} \\ k_{Rr} &= \frac{2E_f I_f}{L_f D_f}\end{aligned}\tag{3.29}$$

The rivet stiffnesses must be integrated over the width of the diameter. These are again integrated using the proposed displacement function and the rotation thereof, as per equation (3.30) where  $x_f$  is the location of the center of the fastener.

$$\begin{aligned} U_{Re} &= \frac{1}{2} \int_{x_f - D_f/2}^{x_f + D_f/2} k_{Re} (v(x))^2 dx \\ U_{Rr} &= \frac{1}{2} \int_{x_f - D_f/2}^{x_f + D_f/2} k_{Rr} \left( \frac{dv}{dx} \right)^2 dx \end{aligned} \quad (3.30)$$

### 3.6 Total potential energy

As stated earlier, the total potential energy of the system is given by its elastic energy minus the work done by the system. This leads to a potential energy formulation given by equation (3.31), which includes the bending energy of the laminate, the extension and rotation in the adhesive layer, the extension and rotation in the fastener, and the work done by the force. The work is described using the displacement field, per equation (3.14).

$$\mathbf{\Pi}_p = U_{lam} + U_e + U_r + U_{Re} + U_{Rr} - W \quad (3.31)$$

To completely write the potential energy equation, the formulations of equations (3.14), (3.16), (3.26) and (3.30) can be substituted to give the potential energy equation dependent on the total displacement function.

$$\begin{aligned} \mathbf{\Pi}_p &= \frac{1}{2} \int_0^{L_0} E_x I_H \left( \frac{d^2 v}{dx^2} \right)^2 dx \\ &+ \frac{1}{2} \int_a^{L_0} k_e (v(x))^2 dx \\ &+ \frac{1}{2} \int_a^{L_0} k_r \left( \frac{dv}{dx} \right)^2 dx \\ &+ \frac{1}{2} \int_{x_f - D_f/2}^{x_f + D_f/2} k_{Re} (v(x))^2 dx \\ &+ \frac{1}{2} \int_{x_f - D_f/2}^{x_f + D_f/2} k_{Rr} \left( \frac{dv}{dx} \right)^2 dx \\ &- P \cdot v(x_p) \end{aligned} \quad (3.32)$$

Now that the potential energy is written using the displacement function, it can be rewritten using equations (3.12) and (3.13). The quadratic terms are replaced by multiplying the vectors with their transposes. The work term is multiplied with the transposes for rewriting purposes.

$$\begin{aligned}
\mathbf{\Pi}_p &= \frac{1}{2} \int_0^{L_0} E_x I_H \{\mathbf{c}_i\}^T [\mathbf{N}_{,xx}(\mathbf{x})]^T [\mathbf{N}_{,xx}(\mathbf{x})] \{\mathbf{c}_i\} dx \\
&+ \frac{1}{2} \int_a^{L_0} k_e \{\mathbf{c}_i\}^T [\mathbf{N}(\mathbf{x})]^T [\mathbf{N}(\mathbf{x})] \{\mathbf{c}_i\} dx \\
&+ \frac{1}{2} \int_a^{L_0} k_r \{\mathbf{c}_i\}^T [\mathbf{N}_{,x}(\mathbf{x})]^T [\mathbf{N}_{,x}(\mathbf{x})] \{\mathbf{c}_i\} dx \\
&+ \frac{1}{2} \int_{x_f-D_f/2}^{x_f+D_f/2} k_{Re} \{\mathbf{c}_i\}^T [\mathbf{N}(\mathbf{x})]^T [\mathbf{N}(\mathbf{x})] \{\mathbf{c}_i\} dx \\
&+ \frac{1}{2} \int_{x_f-D_f/2}^{x_f+D_f/2} k_{Rr} \{\mathbf{c}_i\}^T [\mathbf{N}_{,x}(\mathbf{x})]^T [\mathbf{N}_{,x}(\mathbf{x})] \{\mathbf{c}_i\} dx \\
&- P \cdot \{\mathbf{c}_i\}^T [\mathbf{N}(\mathbf{x}_p)]^T
\end{aligned} \tag{3.33}$$

To have static equilibrium, the variation of the potential energy has to be zero, as per the PMPE. When equation (3.33) is examined, variation in the potential energy can only occur with variation of the coefficients  $\{\mathbf{c}_i\}$ . Therefore the derivative of the potential energy can be written using the transposed coefficients.

$$\delta \mathbf{\Pi}_p = \{\delta \mathbf{c}_i\}^T \frac{\partial \mathbf{\Pi}_p}{\partial \{\mathbf{c}_i\}^T} = \{0\} \tag{3.34}$$

The variation in the transposed coefficients can be taken outside of the brackets, as well as the normal coefficient vector for the terms to which they apply, giving:

$$\begin{aligned}
\delta \mathbf{\Pi}_p &= \{\delta \mathbf{c}_i\}^T \left\{ \left[ \int_0^{L_0} E_x I_H [\mathbf{N}_{,xx}(\mathbf{x})]^T [\mathbf{N}_{,xx}(\mathbf{x})] dx \right. \right. \\
&\quad + \int_a^{L_0} k_e [\mathbf{N}(\mathbf{x})]^T [\mathbf{N}(\mathbf{x})] dx \\
&\quad + \int_a^{L_0} k_r [\mathbf{N}_{,x}(\mathbf{x})]^T [\mathbf{N}_{,x}(\mathbf{x})] dx \\
&\quad + \int_{x_f-D_f/2}^{x_f+D_f/2} k_{Re} [\mathbf{N}(\mathbf{x})]^T [\mathbf{N}(\mathbf{x})] dx \\
&\quad \left. \left. + \int_{x_f-D_f/2}^{x_f+D_f/2} k_{Rr} [\mathbf{N}_{,x}(\mathbf{x})]^T [\mathbf{N}_{,x}(\mathbf{x})] dx \right] \{\mathbf{c}_i\} \right. \\
&\quad \left. - P \cdot [\mathbf{N}(\mathbf{x}_p)]^T \right\} = \{0\}
\end{aligned} \tag{3.35}$$

It must be remembered that  $[\mathbf{N}(\mathbf{x})] = [[N^1(x)][N^2(x)][N^3(x)]]$ , which is a row vector of the shape functions. Therefore the multiplication with its transpose results in a square matrix of which the size is the length of  $[\mathbf{N}(\mathbf{x})]$ . This means all the integrals can be rewritten as matrices and the equation can be rewritten into equation (3.36), where the generalized load vector is rewritten as  $\{Q\} = P \cdot [\mathbf{N}(\mathbf{x}_p)]^T$  and  $[K_B]$  is the bending energy matrix. The other subscripts indicate the origin of the matrix.

$$\delta \mathbf{\Pi}_p = \{\delta \mathbf{c}_i\}^T \left\{ \left[ [K_B] + [K_e] + [K_r] + [K_{Re}] + [K_{Rr}] \right] \{\mathbf{c}_i\} - \{Q\} \right\} = \{0\} \quad (3.36)$$

As the beam will be deflected by the force, the coefficients must be nonzero. So, the sum within brackets must be equal to zero. Defining:

$$[\tilde{K}] = [K_B] + [K_e] + [K_r] + [K_{Re}] + [K_{Rr}] \quad (3.37)$$

Equation (3.36) can be written as:

$$[\tilde{K}] \{\mathbf{c}_i\} - \{Q\} = \{0\} \quad (3.38)$$

This is a linear set of polynomial equations, of which the coefficients are the unknown. This can be solved by taking the inverse of the  $\tilde{K}$  matrix:

$$\{\mathbf{c}_i\} = [\tilde{K}]^{-1} \{Q\} \quad (3.39)$$

Now the coefficients are known, they can be used with the shape functions to determine the total displacement function. Rewriting them into equation (3.10) yields equation (3.40). The opening at the loading point  $v(x_p)$  is of special interest and will be used later.

$$\begin{aligned} v(x) &= [\mathbf{N}(\mathbf{x})] \{\mathbf{c}_i\} \\ v(x_p) &= [\mathbf{N}(\mathbf{x}_p)] \{\mathbf{c}_i\} \end{aligned} \quad (3.40)$$

### 3.7 Integration of the matrices over the three domains

$$\begin{aligned} [K_B] &= \int_0^{L_0} E_x I_H [\mathbf{N}_{,xx}(\mathbf{x})]^T [\mathbf{N}_{,xx}(\mathbf{x})] dx \\ [K_e] &= \int_a^{L_0} k_e [\mathbf{N}(\mathbf{x})]^T [\mathbf{N}(\mathbf{x})] dx \\ [K_r] &= \int_a^{L_0} k_r [\mathbf{N}_{,x}(\mathbf{x})]^T [\mathbf{N}_{,x}(\mathbf{x})] dx \\ [K_{Re}] &= \int_{x_f - D_f/2}^{x_f + D_f/2} k_{Re} [\mathbf{N}(\mathbf{x})]^T [\mathbf{N}(\mathbf{x})] dx \\ [K_{Rr}] &= \int_{x_f - D_f/2}^{x_f + D_f/2} k_{Rr} [\mathbf{N}_{,x}(\mathbf{x})]^T [\mathbf{N}_{,x}(\mathbf{x})] dx \end{aligned} \quad (3.41)$$

It is clear that the focus is to determine the  $[\tilde{K}]$  matrix in order to determine the coefficients for the shape functions. The  $[\tilde{K}]$  matrix is a sum of the matrices above.

$$[\mathbf{N}(\mathbf{x})] = [[N^1(x)][N^2(x)][N^3(x)]] \quad (3.42)$$

$$[\mathbf{N}(\mathbf{x})]^T [\mathbf{N}(\mathbf{x})] = \begin{bmatrix} [N^1(x)]^T [N^1(x)] & [0] & [0] \\ [0] & [N^2(x)]^T [N^2(x)] & [0] \\ [0] & [0] & [N^3(x)]^T [N^3(x)] \end{bmatrix} \quad (3.43)$$

It must be remembered that the  $[\mathbf{N}(\mathbf{x})]$  vector and its derivatives are formed out of three sets of shape function vectors, which are zero for regions outside their domains. This will mean all the stiffness matrices will be similar to the form given in equation (3.43). It is therefore easiest to look at the stiffness matrices per domain and combine them afterwards.

$$[K_B^1] = \int_0^{s_1} E_x I_H [N^1(x)]^T [N^1(x)] dx \quad (3.44)$$

To take an example, the bending stiffness matrix of the first domain would be as seen in equation (3.44). This can be done for all three domains, with adjusting the range of the integral to the correct positions of the domain. Similarly, this can be done for the other stiffness matrices.

However when this is done, there is no connection made between the stiffnesses within the three domains, which makes it an unsolvable system. This is the reason the shape functions were re-ordered when determining the order of functions per domain. This node linking will be similar to simple FE analysis methods.

The functions responsible for the displacement and rotation of the right end of the domain were placed as the last two functions. This means the last 2x2 part of the first domain stiffness matrix is determining the displacement and rotation of the right end node, similarly as the first 2x2 part of the stiffness matrix to its right does for its left end node, which is the same position. Since this displacement and rotation needs to be the same, the determined coefficients need to be the same. These 2x2 regions of the matrices were overlapped and added together to create a condensed matrix, with condensed coefficients.

The condensed matrix and coefficients also need to be accounted for in the creation of the work vector  $\{Q\}$  and re-substituting the solved coefficients into their respective shape function sets. The overlapping coefficients of the condensed set need to be used in the shape function sets of both adjacent domains.

The specimen has a hole to provide space for the fastener. This hole must be accounted for in the integration that needs to be done to obtain the overall stiffness matrix. This can be done by specifying the hole as a variation in width,  $b(x)$ .

If the cross-sectional area is taken over the length of the specimen, and it is divided by the constant thickness, the result is the width of the specimen over its length, as shown in figure 3.5. At the location of the hole, there is less cross-sectional area, which leads to a reduction in the respective width.

With the thickness of the specimen half assumed constant, the variation in width due to the hole leads to a variation in the inertia over the length of the specimen. This result in  $I_H(x) = \frac{1}{12}b(x)h^3$  over the hole, as the cross-section is still rectangular, which can be used in the integrations of the stiffness matrices.

The variation of the width can be described using the analytical solution of a circle, however this leads to problems in the solving part of the SA model, in equation (3.39). The analytical description of the width is a square root function, which changes the system of equations, equation (3.38), from only polynomials to a system of polynomials and square root functions. This led to MatLab not being able to solve the system.

Therefore it was chosen to use a parabola to describe the variation in width instead of the analytical description. As can be seen in figure 3.5, the parabola closely approximates the width at the hole. A parabola was chosen as it is the simplest polynomial available to describe the shape.

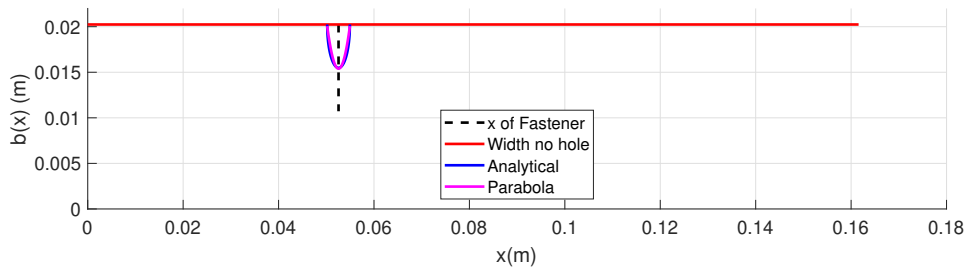


Figure 3.5: Description of the width over the length

As the crack grows through the specimen, there can be a multiple scenarios as to which of the domains the hole is located in, which decides which of domain integrals must be integrated in parts. These scenarios are shown in figure 3.6.

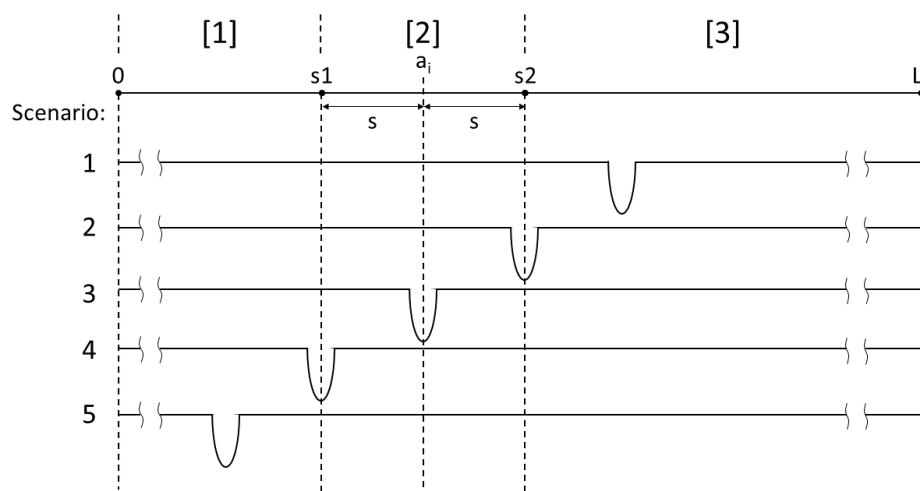


Figure 3.6: Varying scenarios due to the multiple domains, dimensions are not to scale

If the hole is (partially) in a domain, then the stiffness matrix in that domain must be integrated in parts to account for the hole. This is done using a constant width until the hole is reached, using a parabolic description of width for the hole, and again a constant width after the hole for the relevant equations. The ranges of the integrations change as the location of domain 2 is chosen on the location of the crack tip  $a_i$ , as defined in section 3.4.

$$\begin{aligned}
[K_B^1] = & \int_0^{x_f - D_f/2} E_x \cdot I_H [N^1(x)]^T [N^1(x)] dx + \\
& \int_{x_f - D_f/2}^{x_f + D_f/2} E_x \cdot I_H(x) [N^1(x)]^T [N^1(x)] dx + \\
& \int_{x_f + D_f/2}^{s_1} E_x \cdot I_H [N^1(x)]^T [N^1(x)] dx
\end{aligned} \tag{3.45}$$

As an example, if the hole is located in domain 1, shown as scenario 5 of figure 3.6, the example calculation of the bending matrix in equation (3.44) would be a summation of three piecewise integrals, as shown above. From zero to the start of the hole with constant width, where  $I_H$  is a constant. Then over the length of the hole with varying width, where  $I_H(x)$  is dependent on the width. And lastly from the end of the hole to  $s_1$  with constant width and  $I_H$  again.

The foundation and fastener stiffnesses were determined in a similar way. As the location of domain two is determined using the crack tip, there are only foundation stiffness matrices in domain two and three. However, they must still account for the variation in width from the hole, both in integration of the matrices, and in the value of the foundation stiffnesses given by equation (3.17). There is also a difference in the fact that the foundation stiffnesses integrations run from a symbolic crack tip length  $a$  to the end of the specimen.

The difference with the fastener stiffnesses is that they only need to be integrated when the fastener is (partially) in that domain, which is again dependent on the locations of the domains. Eventually a clearance between the hole and fastener was introduced by adjusting the range of the fastener and foundation integrations.

### 3.8 Strain Energy Release Rate (SERR)

When all the stiffness matrices are integrated, accounting for the hole and the fastener location relative to the domain positions, and the coefficients are re-substituted back to obtain equation (3.40), the actual displacement at the loading position,  $v(x_p)$ , is obtained.

The compliance function of the total specimen as a function of the crack length is obtained by equation (3.46). This compliance is a function of the crack tip  $a$  due to the symbolic integration in the stiffness matrices. It should be noted that the opening is multiplied by two to account for the symmetry.

$$C(a) = \frac{2 \cdot v(x_p)}{P} \tag{3.46}$$

The compliance function can be used to determine the SERR, using equation (3.47). If this equation is rewritten using the critical SERR of  $G_{Ic} = 224.9 \text{ N/m}$  to isolate the force, equation (3.48) can be formed. This equation gives the critical load  $P_c$  at a certain crack tip length  $a$ .

$$G(a) = \frac{P^2}{2b} \left( \frac{dC(a)}{da} \right) \tag{3.47}$$

$$P_c = \sqrt{\frac{2bG_{Ic}}{\frac{dC(a)}{da}}} \quad (3.48)$$

It was found that the compliance function of the SA model is not a smooth curve, which will cause problems when taking its derivative for the calculation of the energy release rate. This can be seen as an example in figure 3.7.

In this figure the crack length is located before the fastener, and the red line indicates the compliance function that would be predicted by the Bernoulli theory. As can be seen the compliance function does not follow the expected curve over the full length. However, in the middle domain around the actual crack tip, which in this case ranges from approximately  $0.035 \leq a \leq 0.045$ , the model follows the theory well. This is the case because that is the domain where  $a$  is integrated symbolically.

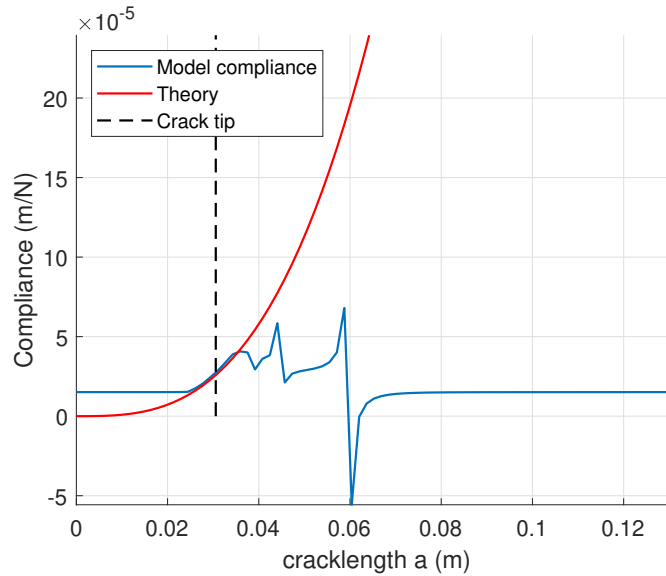


Figure 3.7: Example of the compliance of the model as function of crack tip length.

To account for the issue of the compliance function not being a smooth curve and only producing an accurate description of the compliance in the second domain, it was chosen to fit a polynomial function of the compliance curve, solely in the second domain. For this fitted function a fourth order function was chosen. Initially a third order function was considered, as analytical compliance curves described by Ollsen[10, 32], Carlsson[11], Kondo[33], and Shokrieh[14] are described using third order functions. However, it was found that this led to problems when describing the compliance function around the hole and fastener.

As the crack tip reaches the hole and the fastener, the compliance curve is changed by their presence. The hole increases the compliance significantly in a small area of the function, or the fastener reduces significantly. The third order polynomial could not account for these changes in the compliance function as they were in a short length. It was found the fourth order could account for these changes and was provided more stable functions to be used. Higher order polynomials were also used, but they were found to

not significantly improve the results while increasing the run time of the model.

As can be seen in equations (3.47) and (3.48), the SERR and the critical load depend on the width of the specimen. This width varies around the fastener. The model therefore will change the calculation of the SERR and  $P_c$ , using equation (3.49), when the crack tip is located in between the hole. Note that the crack tip only extends within the laminate and does not penetrate the fastener, thus the critical SERR,  $G_{Ic}$ , need not be adjusted for the presence of the fastener. For the adjustment of the width in equation (3.49), the parabola describing the hole  $b(x)$  was used again.

$$\begin{aligned} G(a) &= \frac{P^2}{2b(x)} \left( \frac{dC(a)}{da} \right) \\ P_c &= \sqrt{\frac{2b(x)G_{Ic}}{\frac{dC(a)}{da}}} \end{aligned} \quad (3.49)$$

### 3.9 Newton Raphson method for crack growth

$$g(a) = \frac{P^2}{2b} \left( \frac{dC(a)}{da} \right) - G_{Ic} = 0 \quad (3.50)$$

The function used to determine the SERR, equation (3.47), is used to derive a function that predicts crack growth. When the  $G_{Ic}$  is subtracted from the SERR function, the function  $g(a)$ , equation (3.50), is obtained. This function is zero when the crack grows from a certain crack length  $a$ .

For the current critical load force, the crack length is known, thus it is known where the function  $g(a)$  equals zero. When the crack grows, the critical load changes, thus the change in force requires a certain change in crack length.

Because crack growth happens when the equation (3.50) is satisfied, it can be used with a Newton Raphson (NR) iteration scheme to determine the crack growth in the specimen. The idea is to use NR to determine the amount of crack growth,  $\Delta a$ , for a certain change in force. For this model the change in force was set as  $P_{next} = 0.975 \cdot P_c$ , thus  $\Delta P_c = 2.5\%$ .

Note that within the NR iteration scheme the number of the iteration is indicated by superscript  $j$ . This must not be confused with the crack length for the cycle  $a_i$ , where the current cycle of the SA model is indicated by subscript  $i$ .

$$0 = g(a^j) + \frac{\partial g(a^j)}{\partial a} \delta a^j \quad (3.51)$$

$$\delta a^j = -\frac{g(a^j)}{g'(a^j)} \quad (3.52)$$

The basis for NR iteration is given in equation (3.51), which can be rewritten to give the adjustment to the initial guess  $a^j$  as equation (3.52). This adjustment to the guessed length can be repeated until the current iteration of crack length is within a set tolerance of the previous iteration. For this model, the tolerance was set at  $\delta_{tol} = 1\mu m$ .

$$a^{j+1} = a^j + \delta a^j$$

$$a^{j+1} = a^j - \frac{g(a^j)}{g'(a^j)} \quad (3.53)$$

$$\Delta a = a^{NR} - a_i \quad (3.54)$$

When the NR scheme has converged to the new crack length,  $a^{NR}$ , the crack growth for the cycle can be determined. The converged crack length will be taken as the new crack length for the next cycle of the SA model.

The SA model will start a new cycle of crack growth as shown in section 3.2. The new positions of the domains are determined based on the new crack length. With their boundaries the new shape functions sets are determined. After which the calculation cycle is repeated from equation (3.33).

This cycle is repeated to calculate the crack growth throughout the DCB specimen. As stated in section 3.2, the crack growth cycles can be stopped using various criteria, such as load, crack tip length or number of cycles. It was chosen to use the critical load, where the model would run until the critical load would get lower than 15  $N$  or higher than 70  $N$ , which were values chosen depending on the experimental results.

The number of cycles that the SA model would take to find the crack growth throughout the specimen is dependent on the change in load,  $\Delta P_c$ . This dictates how far away the next point of calculation is. If  $\Delta P_c$  is made very small, the results from the SA model would be smooth but the calculation time would increase. If  $\Delta P_c$  is larger, the calculation time would reduce, but details would be lost in the results.

As will be seen in the results, the loading force will not always be decreasing during crack growth, so a check was implemented into the model. If there was no converged solution of the NR scheme within 500 iterations, or if the converged solution was a smaller crack length indicating the crack would shrink, the change in loading force would not be decreasing but increasing. Thus, the model would change  $P_{next}$  to  $P_{next} = 1.025 \cdot P_c$ . A similar check was made to ensure converged crack lengths could not be far away from the current crack length, allowing for a maximum crack length increase of 2  $cm$ .

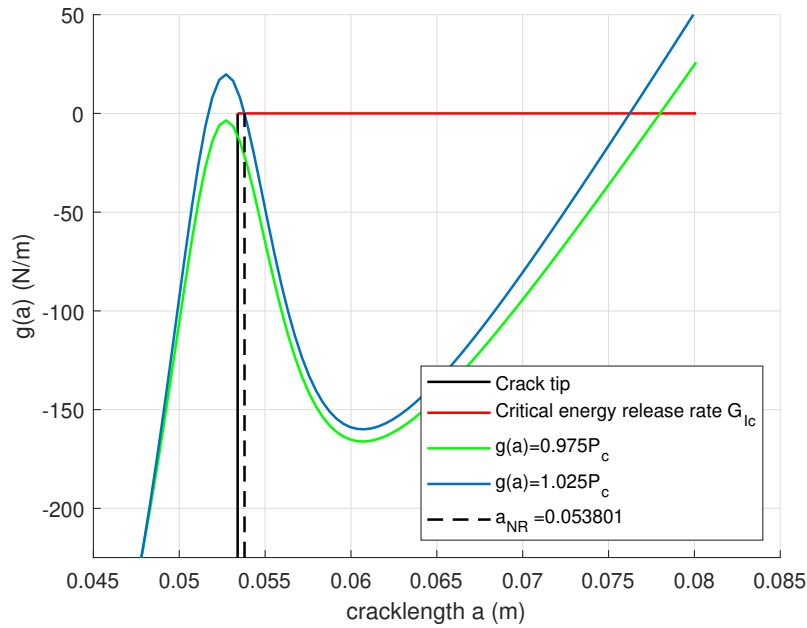


Figure 3.8: Example of the  $g(a)$  function and the implementation of the NR scheme

An example of the NR scheme and the  $g(a)$  functions with different loads can be seen in figure 3.8. The location of the intersection of a  $g(a)$  function with the red line is the increased crack length. As is shown in green, initially a lower force was substituted into  $g(a)$ . However this value does not reach zero, or it does at a crack length far from the current crack tip. Thus, the NR iteration does not converge, or converges to a value far from the current crack tip, which is ruled out by the second check.

After the lower value of  $P_{next}$  does not converge or ruled out, the higher value of  $P_{next}$  is implemented into equation (3.50), as shown in blue. This time the function has two intersections with zero near the current crack tip, and it can be seen that NR converges for a crack length that is larger than the current crack.

There was a possibility of the NR iteration scheme still returning a converged solution of a smaller crack length. Especially around the center of the hole, where the hole is the widest, where a change in crack length in both directions would require an increase of force. Or if a converged solution laid far away from the current crack length. If this was the case, a forced crack length increase of 0.25 mm was implemented. This would normally lead to the next cycle having correctly converged solutions again.

## Chapter 4

# Finite Element model

### 4.1 Base design

The FE model of the test specimen is made in the Abaqus software using the explicit solver. It consists of 5 parts; the upper and lower arms, the cohesive layer, the fastener pin, and the fastener collar. The model was created as a plain DCB model to verify the accuracy of the FE approach. The edges at the end of the specimen in figure 4.1 were used as the loading edges. These edges were constrained in X and Z direction with zero displacement, and a displacement over time in Y was imposed to simulate displacement controlled experiments. The simulation started with zero displacement in any direction. The arms were modelled as solid elements with material orientation and the material properties as given in table 4.1, using the engineering constants option. In chapter 5 the specimen dimensions and materials will be discussed in more detail.

At a distance from the crack tip the elements were approximately 2.5x0.5x1 mm in X-Y-Z. A region with a mesh designed using the 'bias' tool from Abaqus was used to gradually reduce the mesh size in X direction to approximately 0.2x0.5x1 mm at the crack tip. This refined mesh is needed to accurately describe the cohesive layer and crack tip behaviour using the CZM. The elements assigned to the arms were C3D8R type elements from Abaqus' explicit element set, which are 8 node brick type elements with reduced integration to which enhanced hourglass control was assigned.

Table 4.1: Laminate material data [34, 35]

Property	Value	Unit
$E_1$	129.5	GPa
$E_2$	9.37	GPa
$G_{12}$	5.24	GPa
$G_{23}$	3.19	GPa
$\nu_{12}$	0.267	-
$\nu_{23}$	0.4687	-
$G_{Ic}$	224.9	J/m <sup>2</sup>
$\rho$	1580	kg/m <sup>3</sup>
$t_{ply}$	0.19	mm

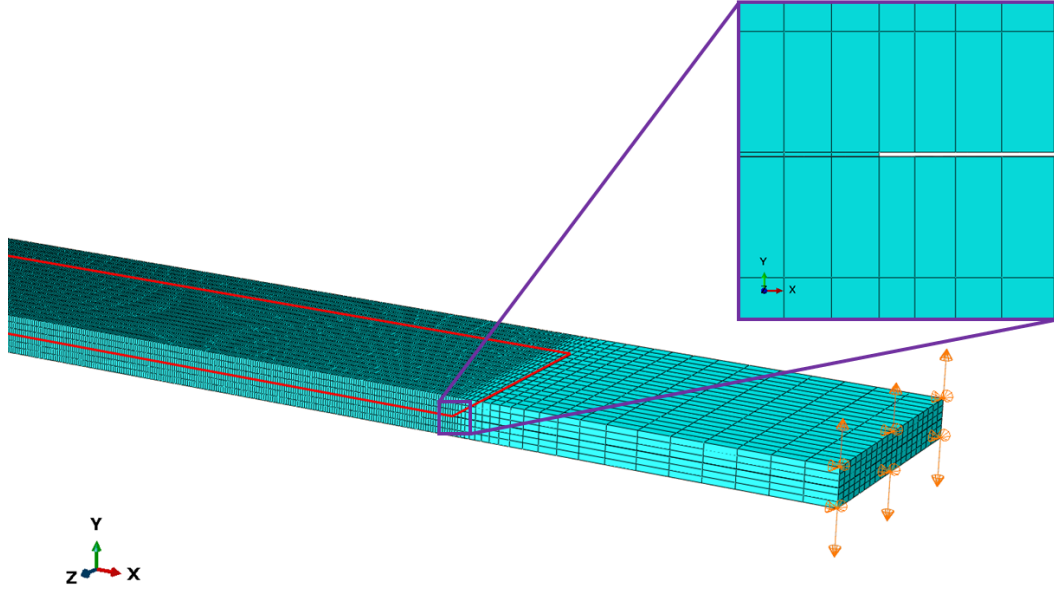


Figure 4.1: Model of the plain DCB specimen

The cohesive layer was modelled as a single layer of cohesive elements with a thickness of 0.019 mm, the thickness which is also used for the adhesive in the SA model. The placement of the cohesive in the assembly is shown in figure 4.1 in red. The cohesive is constraint using a surface-to-surface Tie constraint. Enlarged in the purple square is a side view of the initial crack tip.

The mesh of the cohesive region was similar to the arm, except for the bias region. The bias region was not necessary as the crack tip starts directly at the cohesive. The elements assigned to the cohesive region were COH3D8 type elements from Abaqus' explicit element set, which are node brick type cohesive elements. The material assigned to the cohesive region was assigned traction based elastic behaviour, using the material properties as given in table 4.2. Furthermore the material was given damage behaviour using the Quads damage function of Abaqus, which assumes damage when the value of the quadratic function described in equation (4.1) using the nominal stress ratios reaches one. The fracture behaviour was further implemented using the Damage evolution function using energy based linear degradation of the element, using Power law, given in equation (4.2), to describe the mix mode behaviour with fracture energy coefficients as determined by Endo[35].

$$\left\{ \frac{\langle \sigma_I \rangle}{\sigma_I^o} \right\}^2 + \left\{ \frac{\sigma_{II}}{\sigma_{II}^o} \right\}^2 + \left\{ \frac{\sigma_{III}}{\sigma_{III}^o} \right\}^2 = 1 \quad (4.1)$$

$$\left( \frac{G_I}{G_{Ic}} \right)^\alpha + \left( \frac{G_{II}}{G_{IIc}} \right)^\beta = 1 \quad (4.2)$$

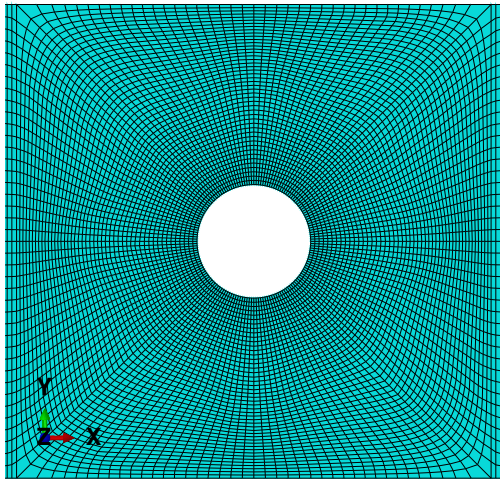
Table 4.2: Epoxy material data [8, 9]

Property	Value	Unit
$E$	2.97	GPa
$G$	1.08	GPa
$\sigma_I^0$	50	MPa
$\sigma_{II}^0$	100	MPa
$\sigma_{III}^0$	100	MPa

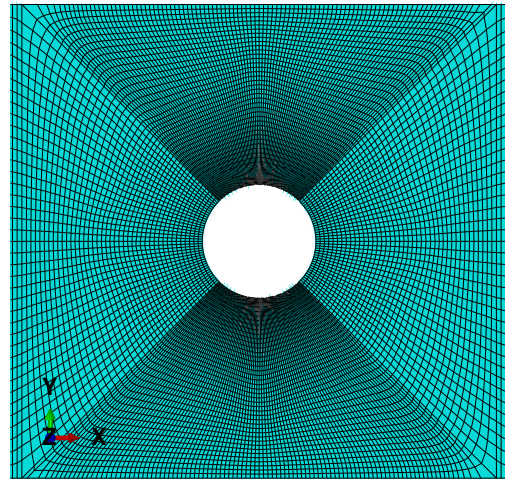
## 4.2 Implementation of the hole

After FE model of the plain DCB specimen was confirmed to be accurate, a model of a DCB specimen with a hole was made. The implementation of the hole meant a need for mesh refinement in the region of crack growth. The surface of both the arms and the cohesive layer was divided into multiple regions to help to control the placement of seeds to improve the mesh around the hole.

Two variations of mesh refinement were made around the hole, a homogeneous and an optimized mesh. The homogeneous mesh was made first, however it gave inaccurate results. The meshed elements were increasing in size the further away from the hole they were located. These bigger elements could not simulate the cohesive zone accurately as can be seen in figure 4.2a. The elements were increasing in size in both X and Y direction. But as the crack growth direction was the X direction, this increase in size led to inaccuracies.



(a) Homogeneous mesh around the hole



(b) Optimized mesh around the hole

Figure 4.2: Meshes refinement around the hole

As stated by Hallet[6], a certain size of refined mesh in crack growth direction is needed to accurately model the cohesive zone. The total mesh size could be decreased. However, as the mesh needed to connect properly to other regions of the model, this would lead to a mesh refinement over the full specimen, which would drastically increase the total

number of elements, and thus increase the run time of the simulation.

It was therefore chosen to find an optimized mesh refinement around the hole. The mesh was refined in the direction of the crack growth, the x direction in figure 4.2b. This led to accurate results, without increasing the number of elements so much that the run time would be increased to the point that homogeneous refinement would be preferred.

Table 4.3: Mechanical properties of the fastener [9]

Part	Material	E (GPa)	$\nu$
Pin	Ti 6AL-4V	114	0.33
Collar	302 stainless	193	0.25

### 4.3 Implementation of the fastener

The fastener was made from two parts, the pin and the collar. The properties used to model these parts are given in table 4.3. The parts are modeled according to the dimensions given by LISI Aerospace[36, 37].

The pin and collar are both made from revolved sketches. The pin is comprised out of mostly C3D8R brick elements with a number of C3D6 wedge elements needed for the inner section around the revolving axis. The part was seeded with a seed size of 0.5 mm and 2988 elements were made within the pin, from which 576 are wedge elements.

The collar is completely made from C3D8R brick elements as the revolving axis does not lie within the part. The seed size was again set at 0.5 mm and the collar is made with 432 elements.

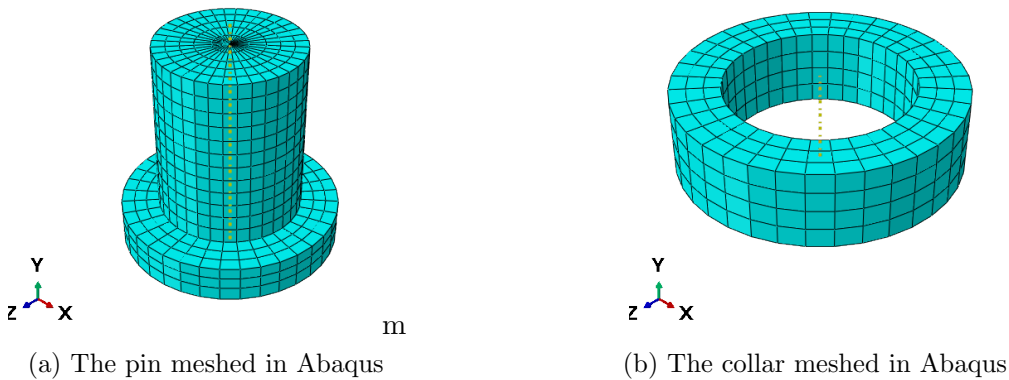


Figure 4.3: The pin and collar

The pin and collar were combined using a tie constraint between the inner surface of the collar and the shaft of the pin. A tie constraint was chosen as this made the placement of the collar easier, such that the collar could be placed on the surface of the laminate. It is simulating a loosely tightened nut, where the nut is clamped against the laminate,

but does not exert a force on the laminate.

There are four interfaces which need to be defined before the model is complete. These are the contact interfaces between the fastener and the DCB specimen. The first is between the shoulder of the pin and the laminate. The second is between the bottom side of the collar and the laminate. The third and fourth interfaces are between the shaft of the pin and the sides of the holes of both arms of the DCB specimen. An argument could be made to have a similar interface between the shaft and the sides of the hole in the cohesive layer, but as this area is insignificantly small compared to sides of the holes in the arms, it was chosen to ignore it for simplicity.

The contact properties of these interfaces were defined using the Surface-to-Surface explicit contact definition in Abaqus. The penalty contact method was used with 'Hard' normal contact behaviour and frictionless tangential behaviour. De Melo[9] had shown that there was so significant difference of modeling a preload or friction on the behaviour of the fastener, thus it is chosen to not do so for simplicity.

In figure 4.4 an overview is given of the FE model of the DCB specimen including fastener. Again with the loaded edges indicated in the bottom right and the location of the cohesive indicated in red. The cohesive is again constraint with a Tie constraint to the upper and lower arm. The materials used for the arms and the cohesive are the same as those used in section 4.1. The model has displacement assigned as loading condition which starts at rest, at zero.

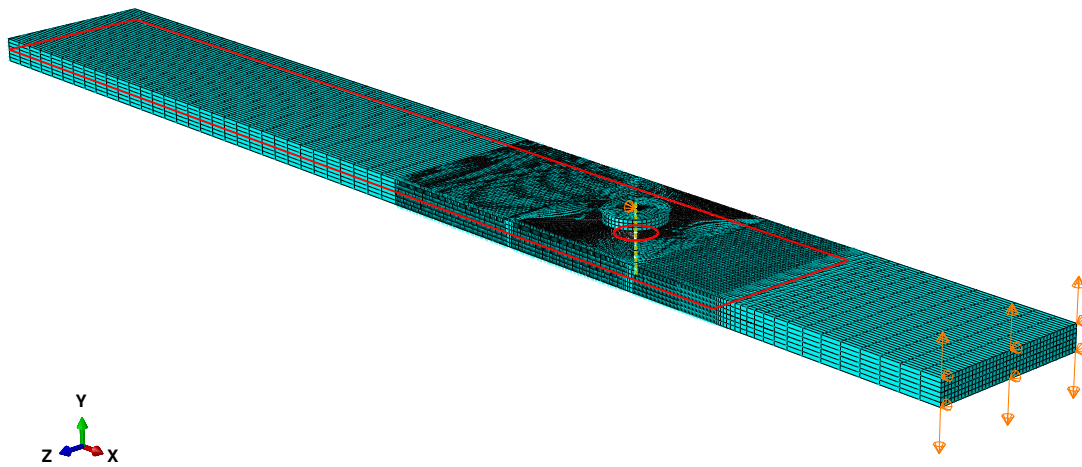


Figure 4.4: Overview of the FE model of a full DCB specimen with fastener

## 4.4 Simulation settings & parameters

This concludes the basic set up of the FE model. There are however other settings and parameters that need to be addressed before the simulation can be run. The performance and run time of the explicit solver is significantly dependent on these factors.

The explicit step was defined as a 1-second step. The incrementation of the step was kept automatic and mass scaling was used to reduce the computational time. The FE

model contains a large amount of elements with critical time steps of values smaller than  $1 \cdot 10^{-8}$  second. The mass scaling was set to apply to the whole model at every increment with a target time for the increment of  $1 \cdot 10^{-6}$  second. The amplitude used for the displacement was a linear increase from 0 to 1.

The mass scaling used to increase the increment time was critical to reduce running time of the simulation, in particular the target time. There was no optimization done to determine the fastest simulation of the model. However, the target time was slowly increased over the multiple runs of the model done during development to reduce the amount of increments made and therefore reduce the run time. The initial target value during development of the model was  $t = 1 \cdot 10^{-7}$ . It was continuously checked if the produced results would still be accurate. It was found that when the target time was increased to  $t = 2 \cdot 10^{-6}$  the results would begin to be distorted by harmonic noise. Therefore it was chosen not to increase the target time further than  $1 \cdot 10^{-6} \text{ sec}$ .

The designated history and field outputs settings are important to the results and the interpretation thereof. The field output request was adjusted from default by increasing the frequency to an output every 0.01 second and requesting the SDEG and STATUS variables for the behaviour of the cohesive layer. The default history output settings were kept the same, except for the recording frequency, which was increased to match the field output.

Next to the default history output two separate history output requests were made. One was made for the reaction forces on the nodes on one of the displacement edges, and one was made for the displacement of a node on that edge. They vary from the other output requests in that their output was set to an even higher frequency. The time step of every output was set at  $1 \cdot 10^{-4}$  second. This time step was set so small to be able to obtain a smooth output curve for the force-displacement plots and to allow for filtering of the results.

It was also found that the contact between the fastener and the specimen would introduce vibrations and harmonic noise in the simulation. This was caused by the frictionless tangential behaviour and the clearance between the fastener and the hole. This caused the fastener to bounce around within the hole until it was clamped into position by the opening of the specimen arms. However at this point the whole model would be vibrating, which would not fade as there was no dampening modelled in any of the parts or materials. This was solved by removing the X constraint on the loading edges of the arms and introducing an X constraint on the center point of the pin head for the FE model with the fastener. This is shown in figure 4.4. This kept the fastener in its place until it was affected by the opening of the laminate, and thus reduced the vibrations.

## Chapter 5

# Results

In this section the results of the SA model will be discussed. Depending on which type of DCB test is simulated, the SA results will be compared with theoretical models, FE analyses, and/or experimental data, which was provided by Bastiani[34].

The SA model was developed in three stages; a plain DCB specimen, a DCB specimen with a hole implemented, and a DCB specimen with a hole and an installed fastener. Therefore, the results will also be discussed respectively in those stages.

### 5.1 Specimen Details

The models were developed around a specimen with a single set of dimensions. The dimensions were adjusted to match with the specimens used in the experiments executed by Bastiani[34].

The specimens used in that study were in agreement with the ASTM standard D5528-13 [38], with the exception of the initial crack length  $a_0$ . Though the  $a_0$  was not equal to the recommended value, it was within the accepted range of the ASTM standard.

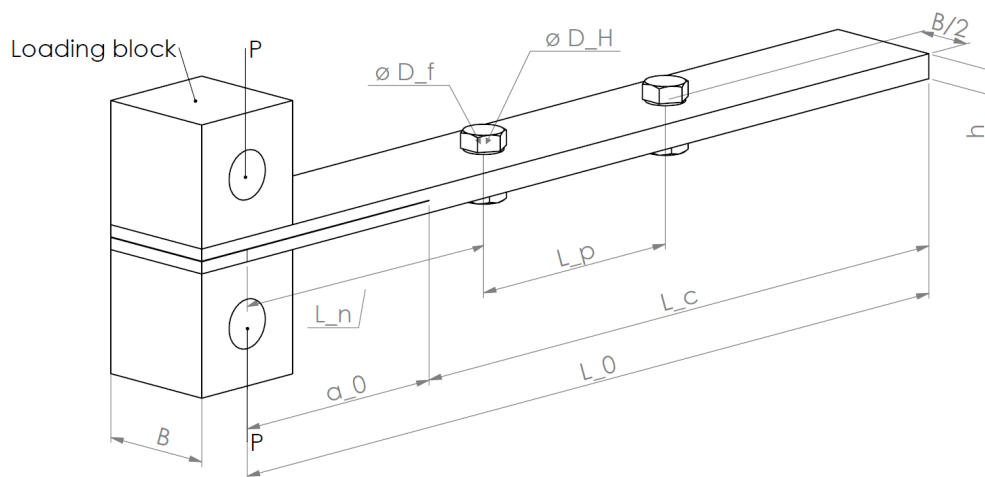


Figure 5.1: Overview of the test specimen and its dimensions

The schematic overview from figure 5.1 is adjusted from the ASTM standard to allow for the presence of fasteners in the test specimen. The distance from the loading points until the first fastener is indicated as  $L_n$ , the distance between fasteners would be indicated as  $L_p$ , the diameter of the fastener as  $D_f$ , and the hole as  $D_H$ . For now the number of fasteners will be taken as 1. The crack length  $a_0$  is taken from the loading point as the material in front of the loading point does not deform, and it simplifies modelling significantly in both the SA and FE model.

The dimensions used for modelling the specimen are given in table 5.1 and are mostly adapted from Bastiani[34]. They are adjusted to account for half the width of the loading block. The fastener dimensions are adapted from De Melo[9].

Table 5.1: Dimensions of the specimen ( $mm$ )[34]

$L_0$	$b$	$h$	$a_0$	$L_n$	$D_f$	$D_H$	$B/D_f$
161.5	20.24	3	31.5	52.5	4.76	4.85	4.25:1

## Material

In accordance with the ASTM standard the specimen is a unidirectional, or UD, layup. The material is a carbon epoxy material system, with properties that are typical for aeronautical structures.

The material system that will be modelled is the Hexcel<sup>®</sup> AS4/8552 system, of which the material properties are given in table 4.1. The specimens were modelled as a 16 layered, or  $[0]_{16}$ , laminate, with the crack tip symmetrically splitting the laminate.

The material that is used, has been investigated by Endo[35] and Bastiani[34]. The critical SERR's,  $G_{Ic}$  and  $G_{IIc}$ , were experimentally determined by Endo for mode I, mode II, and mixed mode behaviour with varying temperatures. For the temperature ranges observed, a relation using the power law criterion was obtained. The  $G_c$  for mode I was later experimentally determined again by Bastiani, using DCB testing for various set-ups.

Table 4.1: Laminate material data [34, 35] (repeated from page 31)

Property	Value	Unit
$E_1$	129.5	GPa
$E_2$	9.37	GPa
$G_{12}$	5.24	GPa
$G_{23}$	3.19	GPa
$\nu_{12}$	0.267	-
$\nu_{23}$	0.4687	-
$G_{Ic}$	224.9	J/m <sup>2</sup>
$\rho$	1580	kg/m <sup>3</sup>
$t_{ply}$	0.19	mm

For modelling the epoxy material, or the cohesive, in the FE analysis, its properties must be determined. The values used by Donadon[8] and de Melo[9] were adopted and are

given below.

Table 4.2: Epoxy material data [8, 9]  
(repeated from page 33)

Property	Value	Unit
$E$	2.97	GPa
$G$	1.08	GPa
$\sigma_I^0$	50	MPa
$\sigma_{II}^0$	100	MPa
$\sigma_{III}^0$	100	MPa

Table 4.3: Mechanical properties of the fastener [9] (repeated from page 34)

Part	Material	E (GPa)	$\nu$
Pin	Ti 6AL-4V	114	0.33
Collar	302 stainless	193	0.25

To enable modelling of the fastener in the SA model only the elastic modulus of the fastener will be necessary. However, in FE modelling the simplest linear elastic material requires the Poisson's ratio of the material as well. It was chosen to follow the pin and collar modelling of the fastener, as used by de Melo[9]. These are standardized parts, which are also used in the study performed by Bastiani[34], The difference between these studies is that Bastiani uses an aluminium collar. However, as the loaded area of the collar is larger than the shaft of the pin, it is assumed the shaft will be the location of material deformation, no matter the collar material selection. In the SA model only the pin material will be used.

### Other parameters used for the models

Most of the parameters used for the SA model are mentioned above while describing the specimen. Other parameters which were used which value have not been mentioned or needed to be calculated will be listed below.

Table 5.2: Parameters used for the Bernoulli theory

$G_{Ic}$	$B$	$E$	$I_H$
224.9 $J/m^2$	20.24 $mm$	129.5 GPa	5.6925 $mm^4$

Table 5.3: Other parameters used in the SA model

$s$	5 $mm$	$h_H$	1.5095 $mm$
$\bar{E}_x$	128.9 GPa	$x_f$	52.6 $mm$
$I_H$	5.6925 $mm^4$	$E_f$	114 GPa
$\bar{E}_y$	12.0 GPa	$A_f$	17.795 $mm^2$
$\bar{G}_{xy}$	5.21 GPa	$L_f$	3 $mm$
$L_c$	131 $mm$	$D_f$	4.76 $mm$
$k_e$	$3.194 \cdot 10^{11} \frac{N}{m}/m$	$k_{Re}$	$2.787 \cdot 10^{11} \frac{N}{m}/m$
$k_r$	$6.726 \cdot 10^4 \frac{N}{\theta}/m$	$k_{Rr}$	$8.506 \cdot 10^5 \frac{N}{\theta}/m$

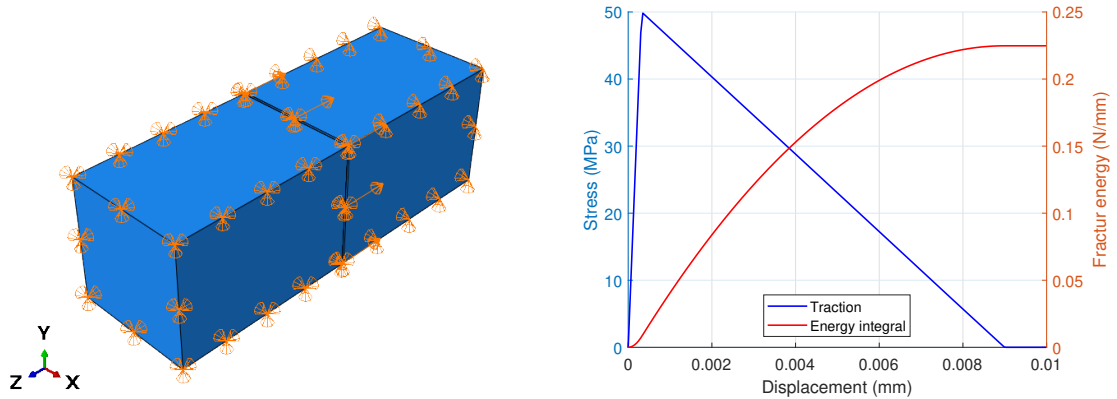
## 5.2 FE model validation

To validate the cohesive modeling, the approach of the traction separation curve was taken. The correct model behaviour of the adhesive is dependent on its fracture energy, which should be the same as the critical SERR of the material. This is tested by a pull test of a 1x1 mm element of the cohesive. The model is made with laminate material at both sides which are either locked in place or given a displacement. The cohesive element in the middle is constraint with tie constraints to the surfaces of both laminate pieces. The model is shown in figure 5.2a.

The element will be pulled apart during which the stresses within and displacements of the element will be noted. This will give a traction separation curve of the cohesive, of which the area under the curve can be integrated to determine the fracture energy. If the material is modeled correctly, the fracture energy at the end of the separation will be the same as the critical SERR.

As can be seen in figure 5.2b, the cohesive material starts to fail at 50 MPa, as given by table 4.2. The material has fully failed at a displacement of  $\delta_f = 9.038 \mu m$ . If the points of this graph are integrated for example using the Trapz function in MatLab, the value of  $G_{Ic}^{FEM} = 0.2249 N/mm$  is obtained. This is the same as the  $G_{Ic}$ , when converting to meters, therefore the cohesive is displaying the correct behaviour.

As the fastener is modelled using simple linear isotropic materials, which should not display any failure or damage, it was chosen not to validate the fastener.



(a) Overview of the cohesive element test model (b) The traction separation curve given by the cohesive element

Figure 5.2: Validation of the cohesive material modelling

The next step was to run the FE model for the plain DCB specimen, to be able use its results to compare to the SA model. The FE model is compared against the Bernoulli opening theory of section 3.1. The reaction force ( $P$ ) and opening displacement ( $v$ ) at the loading edges of the plain DCB specimen, without a hole or fastener, were read and stored during the time-step simulated in the FE analysis, as described in section 4.4.

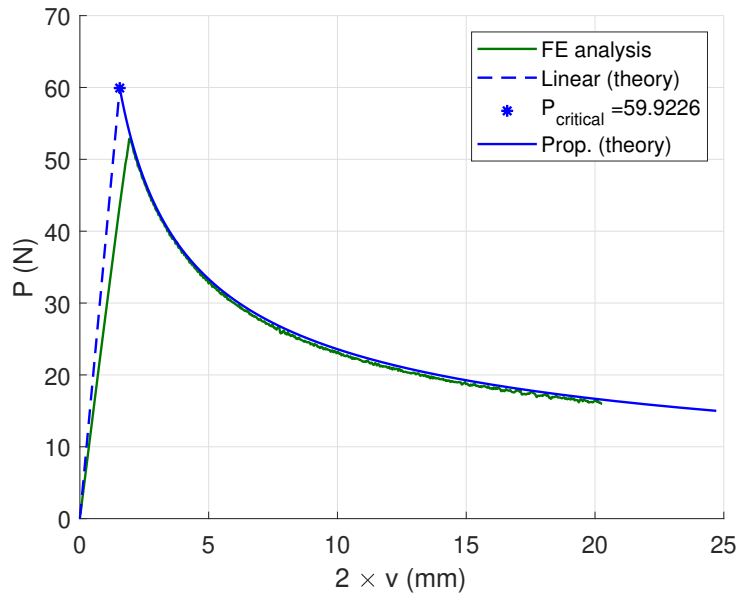


Figure 5.3: Comparison of the FE analysis to theoretical values

The force and displacement were filtered using a Decimation filter, to reduce the amount of data points for handling purposes and to reduce noise. The noise made it difficult to interpret the model behaviour when the hole and fastener were implemented. A comparison between the raw and filtered data can be found in appendix A. After which they were plotted against the Bernoulli theory, which can be seen in figure 5.3.

It has to be noted that the opening displacement on the x-axis in the plot is the total opening displacement, from the top arm from the specimen to the lower arm, thus it is indicated as  $2 \cdot v$ . The linear theory is the line described by equation (3.1) in section 3.1, and the crack propagation, or Prop., is equation (3.6).

As can be seen, during the linear elastic opening, the FE model predicts more compliance than expected by the Bernoulli beam theory. This is to be expected as the theory assumes a solid clamped boundary condition for the arms from the crack tip to the loading edge. This is not a perfectly realistic assumption as the material in front of the crack has the same elastic material properties as the rest of the arm, thus it is an elastic base. This was also extensively discussed by Olssen[10].

The propagation curve of the FE model is almost identical as predicted using equation (3.6). From this point on, the FE model is assumed verified.

### 5.3 Plain DCB

In figure 5.4 the results of a plain DCB specimen in the SA model are visible, plotted against theoretical curves. These theoretical curves are obtained using the derivation using Bernoulli beam equations as shown in section 3.1.

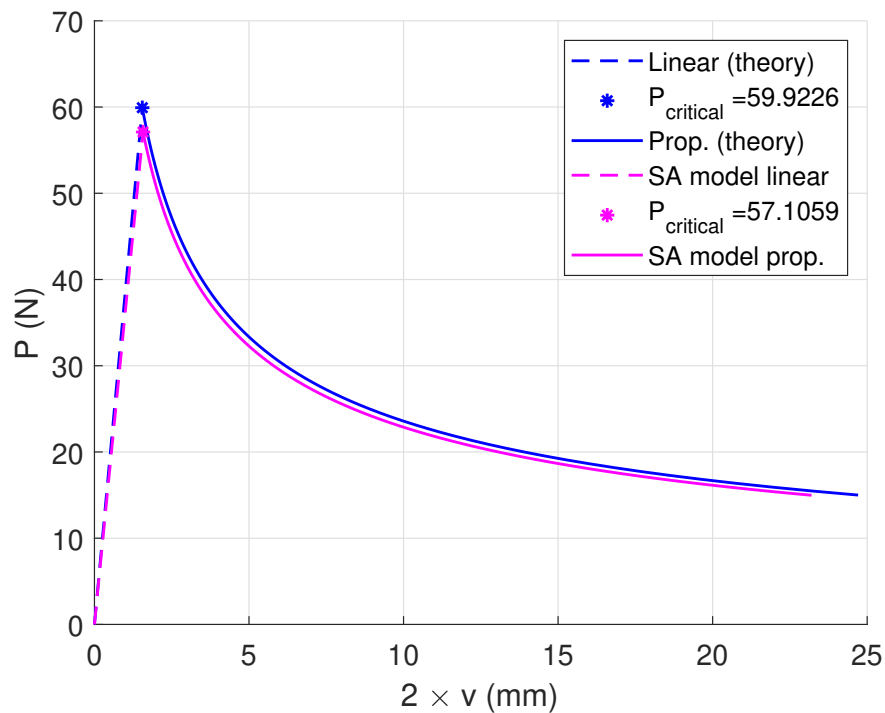


Figure 5.4: Plot of the SA model of a plain DCB specimen against theory

As can be seen the linear behaviour follows the theoretical linear behaviour, while being slightly more compliant. The opening displacement at initial crack growth is  $1.572 \text{ mm}$  and the theoretical expectation is  $1.548 \text{ mm}$ . However, a better comparison for compliance would be the difference at a set force. At a force of  $40 \text{ N}$ , the theory would expect an opening of  $1.033 \text{ mm}$ , and the SA model predicts an opening of  $1.101 \text{ mm}$ . This is a difference of  $6.58\%$ , however not as compliant as the FEA.

The difference in the critical loading is also noticeable, but remains small. The difference at the start of the crack growth is  $2.82 \text{ N}$ , which is a difference of  $4.7\%$ . This is remarkably close since the determination of the critical load is dependent on the derivative of the polyfit approximation of the compliance function.

The crack propagation behaviour of the SA model mimics the propagation behaviour of the theory well. The offset between the SA model and the theory seems to be consistent throughout the propagation. It may seem that the offset between the models is large at the end of the curve. However, the models were stopped at forces lower than  $15 \text{ N}$ , independent of crack length or opening displacement.

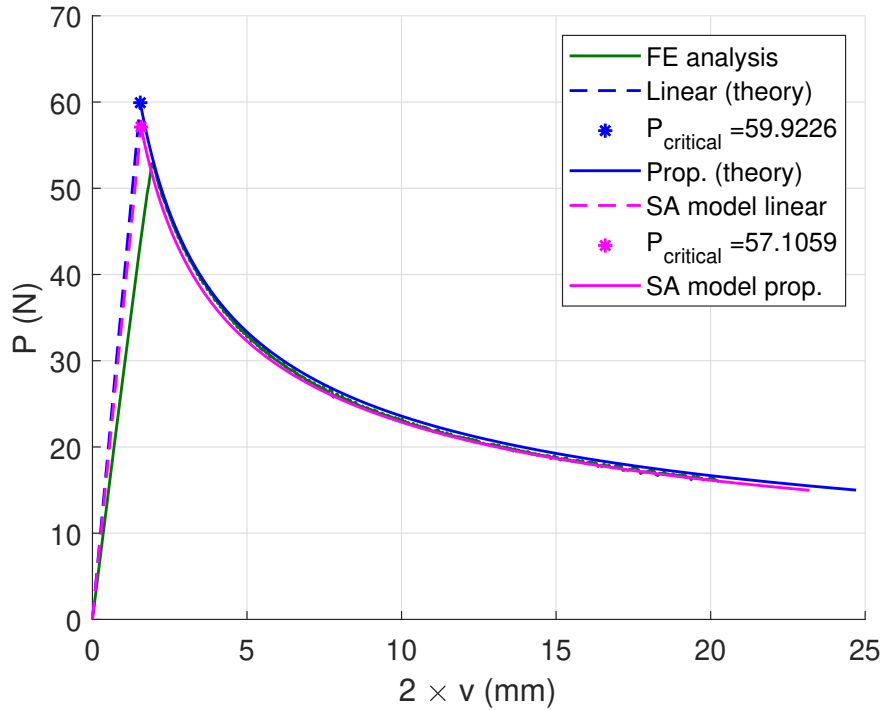


Figure 5.5: Comparison of the SA model of a plain DCB specimen with theory and FEA

In figure 5.5 the force displacement curve of the FE analysis is added to the plot. Similar to the validation of the FE model in section 5.2, the main difference between the models is the linear opening behaviour. The propagation behaviour between the models is virtually identical, where the FE analysis splits the narrow difference between theory and the SA model.

In the FE validation section this more compliant behaviour of the FE model has already been discussed. It was stated that the assumption of the perfectly clamped beam for the Bernoulli equations in the theoretical equations was the main culprit behind this difference, as discussed by Ollsen[10]. However, the expectation was that the SA model would allow for a combination of small displacement and rotation at the base of the crack tip. This would simulate the elasticity of the base material as the FE analysis suggest. However, as the SA model does simulate a more compliant behaviour than theory, one could argue that it indeed allows for those deformations at the crack tip, but this behaviour is not as severe as the FE analysis.

## 5.4 DCB with a hole

The next phase of development of the SA model was the implementation of the hole within the specimen for the placement of the fastener. This is also the aspect where the theoretical or analytical models stop. There currently is no model to describe the propagation of the crack through a DCB specimen with a hole. Therefore, from this moment on, shall the SA model only be compared to the FE model and experimental

data.

The experimental data was provided in sets of three experiments. For comparison with the SA model and the FE model only the first experiment of the three is used. If the SA model is compared to only experimental values, all three curves within the set are used.

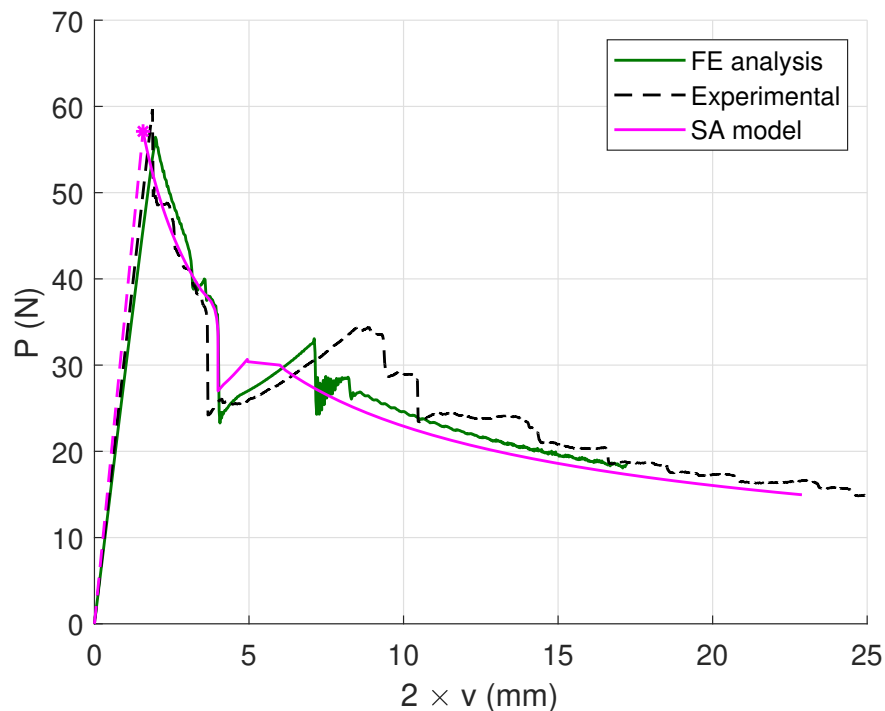


Figure 5.6: Comparison of the SA model of a DCB specimen with a hole with FEA and experimental data

In figure 5.6 the force displacement curves can be seen of the SA model compared to a FE analysis and experimental values. All three have a similar linear behaviour and an almost identical initial critical load. What is remarkable about this, is that the linear behaviour of the FEA seems different, compared to the previous results shown of the FE model. This is also visible in the first region of the crack propagation, where the force per opening of the FEA is slightly higher than the experimental en SA values. It is thought to be similar to crack tip sharpening in the experimental data[34]. However it is unknown why it does happen in this FE simulation and why it has not in the others.

Nevertheless, the SA model mimics the experimental values well. Its linear behaviour is roughly identical, though slightly stiffer. The initial critical load of the experiment is higher than the SA model, however this can be explained by crack tip sharpening.

The experimental specimens are prepared using a PTFE (polytetrafluoroethylene) insert to create the initial crack. This leaves a very blunt area with an increased volume of epoxy resin at the crack tip. Therefore, before the crack can propagate, the crack tip needs to sharpen to increase the stress concentration factor at the crack tip. This leads

to higher initial loads to start the crack propagation.

After the crack propagation has been initiated, the crack propagation of the SA model and the experiment are matching. The force reductions over the opening follow the same path, and they are laying over each other until the crack reaches the hole in the specimen. What can also be seen is that just before the hole the FE curve returns to values similar to the SA model and the experiment.

The crack tip reaches the hole at an opening of approximately 4 *mm*. This can be seen by the sudden vertical drop in force at that opening displacement. This snap through behaviour is originating in the reduction of the width by the hole. It is clear in figure 5.6 that this snap through is happening at identical displacements for the FE and SA models. The experiment has a slightly lower opening displacement but remains comparable.

This snap through is linked to the SERR as calculated by equation (3.49), repeated here below. The reduction in width has two effects. The SERR calculated at that crack length becomes larger than at a specimen with constant width, thus crack growth happens more rapidly. It also means the critical load  $P_c$  at that crack length becomes smaller, which in turn results in the critical opening displacement being smaller.

However, the DCB test is a displacement driven test meaning that the opening displacement applied to the specimen will not get smaller. Which means the specimen at this crack length is loaded higher than its critical load and opening, which means the crack will continue growing, or snaps through.

This patch of uncontrollable crack growth stops when the crack tip has reached a length where the critical opening displacement is the same as the start of the snap through but the critical load is the smallest. After which, the critical load needs to increase again, which means the opening displacement increases again. This increase in the opening displacement is the continuation of the DCB test.

$$G(a) = \frac{P^2}{2b(x)} \left( \frac{dC(a)}{da} \right) \quad (3.49)$$

$$P_c = \sqrt{\frac{2b(x)G_{Ic}}{\frac{dC(a)}{da}}}$$

One could assume the snap through stops at the center of the hole, where the width of the specimen would be the smallest. This is however not the case for the SA model. The lowest value for  $P_c$  is reached when the crack tip reaches a distance approximately 1.1 *mm* after the center of the hole. This is most likely due to the fact that the opening force and displacement are calculated with greater steps than the FE model is recording its forces and displacements. This could also explain the difference in force reduction. It is logical the critical load would increase after the center of the hole as the width increases again. However there are three-dimensional aspects which can not be accounted for in the SA model, as it is a 2D approach.

This has been discussed by De Melo[9] and Bastiani[34]. The most critical one is the crack tip front shape. The different states of the crack tip front are shown in figure 5.7 at multiple moments during the crack propagation, using the FE analysis. The non damaged

cohesive layer is shown in blue, the fully damaged and released cohesive elements are shown in red.

Normal crack propagation in a DCB specimen without holes or fasteners occurs at the moment indicated by I. The crack tip front is straight or slightly curved. This matches the SA model, as the 2D simplification of the DCB specimen assumes a straight crack tip front across the DCB specimen. This changes when the hole is involved.

At the snap through, indicated by II and III, the crack tip front remains relatively straight. This means the SA model can follow the curve predicted by the FEA, and it is shown that the snap through behaviour is happening at an identical opening displacement. At region III the lowest forces are experienced for the FE model when the crack tip front is roughly in the center of the hole.

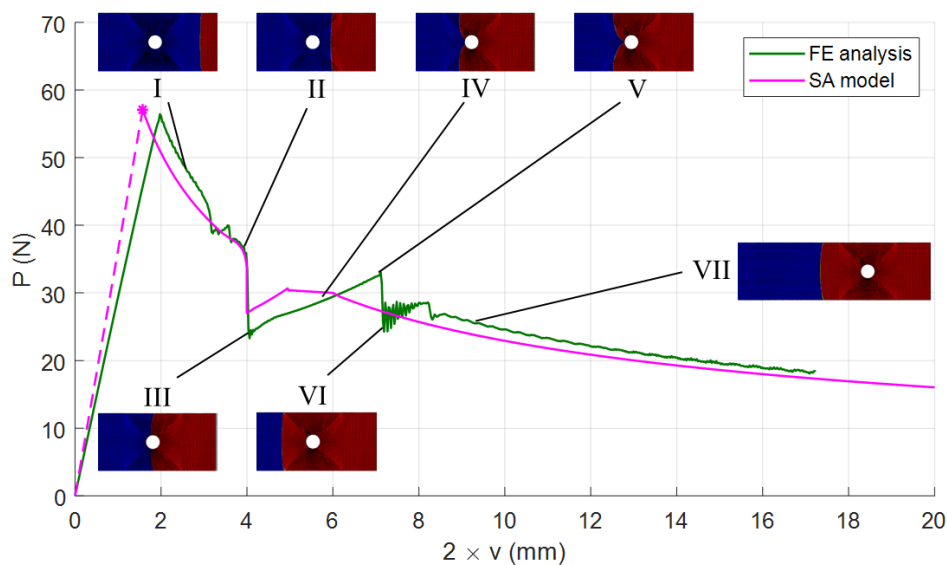


Figure 5.7: Plot of the crack tip front at multiple moment of the FE analysis of a DCB specimen with a hole.

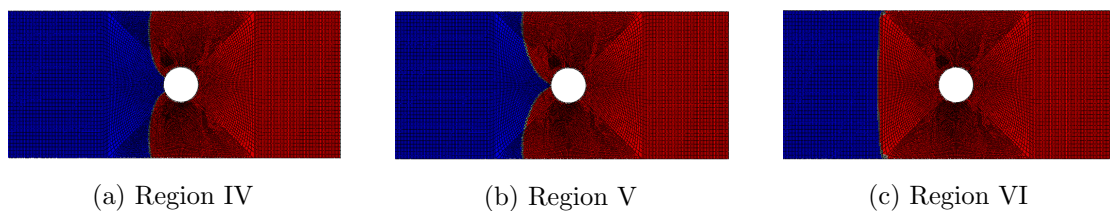


Figure 5.8: Enlargements of regions IV, V, and VI

At the region labelled by IV, the crack tip front reaches the end of the hole. This is the moment where the SA model assumes the crack tip will continue as a straight front, and it continues with regular crack propagation, as shown in the graph. However, what can

be seen between region IV and V, is that the crack tip keeps hanging on to the end of the hole. This change of the crack tip shape at the hole has been seen and predicted by De Melo[9], it has been seen and confirmed by Bastiani[34], and it has two main effects. The first effect of this curvature is increase the total length of the crack tip front, by curving the crack tip from the hole to the sides, which in turn increases the forces necessary to grow the crack tip. This continues until the peak shown by V, which leads to a secondary snap through when the crack tip releases from the hole end to return to a straight edge, as indicated by VI.

The secondary effect is that curvature of the crack tip front also changes the loading mode of the crack tip, as its orientation to the loading changes. This means the crack tip front at the sides of the specimen still experiences mode I opening, while the crack tip front at the hole experiences mixed mode loading, as its orientation is rotated with more than  $45^\circ$ . This rotation increases the opening force as the critical SERR for mode II or III loading is always higher than mode I, thus the locally mixed mode  $G_c$  will be higher than the pure mode I  $G_{Ic}$ . This increased  $G_c$  also contributes to the higher force necessary for continuing the crack growth. It is however difficult to determine which of these two factors is dominant in producing this loading peak after the hole.

When the crack tip front is released from the hole end, it snaps through to VI. This secondary snap through occurs because the point of the crack tip front can now again be loaded in pure mode I. This means the loading force on the arms is higher than is the critical loading  $P_c$  necessary to grow the point of the crack tip front. This increases the crack tip at the point rapidly until it is equal to the rest of the specimen width, as shown by VI.

There is a stabilization period where the exact crack tip shape and location are formed again by the CZM, but afterwards the crack propagation has calmed and continues with regular crack propagation. This is indicated by VII.

In the crack propagation after the hole, the opening displacement at a certain force is larger in the FE model than expected by the SA model. This is due to the presence of the holes in the arms of the DCB specimen. These holes reduce the total inertia of the arm, meaning the deflection is higher for the same load.

This is also the case for the SA model if compared to the SA model for a plain DCB, however it is barely visible. The reduction in width is only present over a small length, compared to the overall specimen length. Thus, when the hole is located in domain 1 or 3, the small length of inertia reduction, combined with the larger domain sizes and the lower order shape function sets for the domains, means that the SA model is less suited to account for this varying inertia. This was similar for the crack tip. This combination of a small area of influence over a long specimen was also the reason to develop the model with multiple domains, to have a more accurate description of the crack tip.

In figure 5.9 below the SA model is plotted against all experimental values found by Bastiani[34]. All the characteristics of the curves which are described above can be found in this graph as well. The linear opening of the SA model being slightly stiffer than all the experimental values. Each of the experimental curves having a initial critical load spike, to sharpen the crack tip from the excess epoxy at the film insert. The crack

propagation of the SA model before the hole being identical to the experiments. The snap through of the crack tip at the hole happening at a comparable opening displacement. The force reduction being larger in the experiments than predicted by the SA model. The SA model assuming normal crack growth after passing the hole. The experiments having a force peak after the hole as the crack tip front is curved by, and hanging onto, the hole. A secondary snap through in the experiments as the crack tip front is released. And continued stable crack propagation with an increase opening due to the holes in the loading arms.

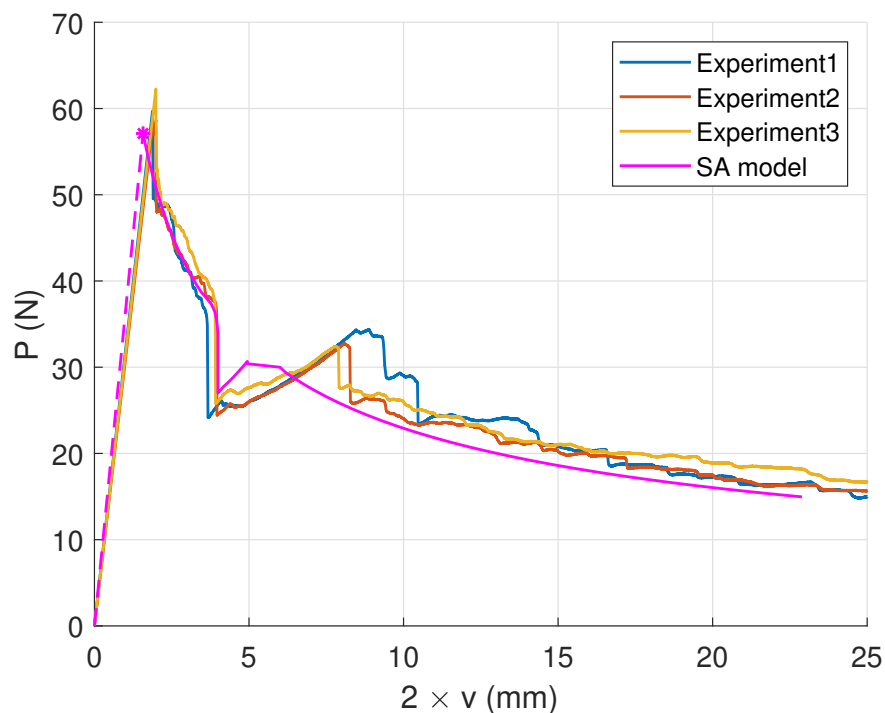


Figure 5.9: Comparison of the SA model of a DCB specimen with a hole with multiple experiments

## 5.5 DCB with a fastener

The final phase of the development of the SA model was the implementation of the fastener in the DCB specimen. Similar to the SA model with the hole, there is no theoretical description for this model. Therefore shall the model again be compared to the FE model and experimental data. It should be noted that all the coming plots are scaled up in horizontal direction compared to previous images due to the fastener response, meaning differences in opening displacements will seem larger.

In figure 5.10 the SA model is plotted against the FE model and one of the experiments. The second half of the plot is to be discussed in stages. For the first half, the results are the same as the plain DCB and the DCB with a hole. The linear opening is stiffer than

both the FE analysis and the experimental values, while the experimental opening is slightly stiffer than the FE analysis. The crack propagation until the fastener is initiated is indistinguishable between the three curves. The crack tip sharpening of the insert epoxy residue can also be seen again in the experimental curve.

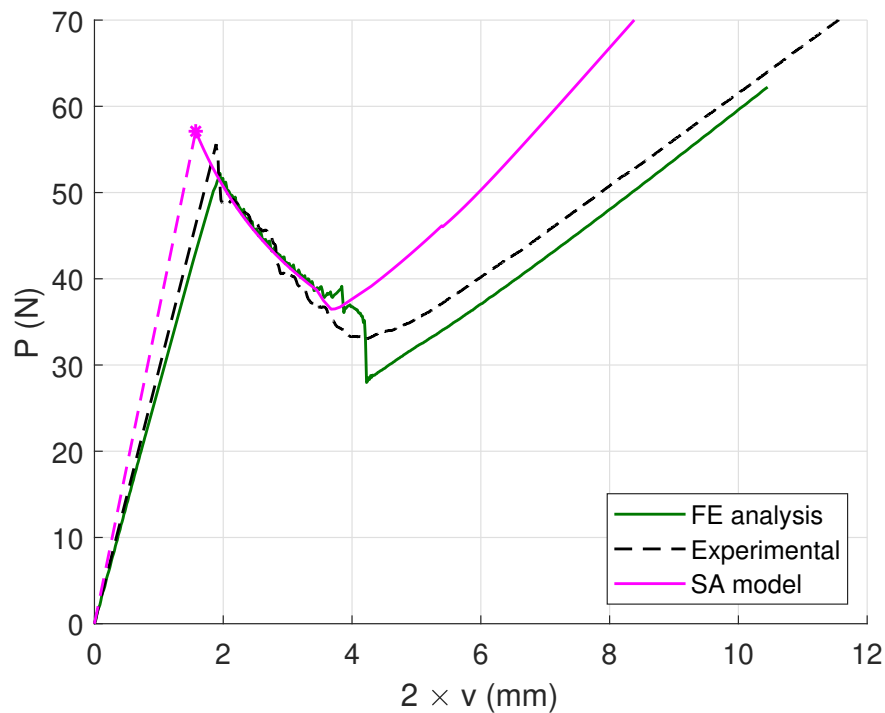


Figure 5.10: Comparison of the SA model of a DCB specimen with a fastener with FEA and experimental data

To discuss the region where the fastener is initiated and all three curves follow different paths, the SA model must be compared against data sets with different parameters. This is done over the next few plots.

Firstly, the FE model has a snap through before the fastener is initiated. This was contrary to the conclusions taken by De Melo[9]. The harmonic noise introduced into his results by the dynamic excitement of the fastener most likely blurs the snap through behaviour in his results. This snap through behaviour is dependent on the preload applied on the fastener, as found by Bastiani[34].

The amount of preload, or absence thereof, determines the moment when the fastener is activated as crack growth arrest mechanism. This is shown in figure 5.11. Bastiani has shown that with higher preload, until nominal preload specified by the supplier, the fastener is activated earlier in the opening of the DCB specimen and does not allow for an area of uncontrollable crack growth, or snap through[34].

Initially it was tried to allow for a similar snap through in the SA model. One method of which was to allow for a clearance between the fastener and the hole. It was thought that this would delay the initiation of the fastener and therefore allow for snap through crack growth. But the altered SA model would give almost identical results. Another

method tried was to alter the length  $s$  of the middle domain. This would again not improve the results significantly.

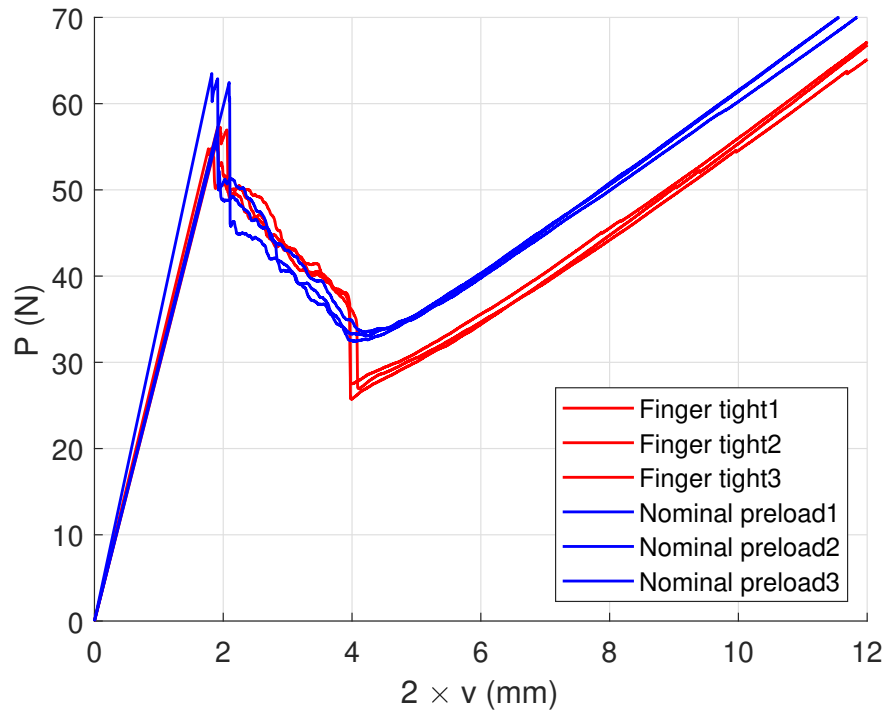


Figure 5.11: Comparison of experiments with fasteners loaded according to the nominal preload and finger tight

Therefore, it is best to compare the SA model to the experiments with nominally tightened fasteners, which is shown in figure 5.12. Again, the crack propagation is identical until the fastener is initiated. The initiation of the fastener is earlier in the propagation of the SA model than the experiments, as the force increase starts at a smaller opening.

The force increase after fastener initiation is deviating from the increase at the experiments. This could be a result of the earlier effects of the fastener. As the crack has not been allowed to grow as far as would have been in the experiments, the opening arm in the SA model would be shorter, which would cause a stiffer opening behaviour, and thus the deviation of the force increase.

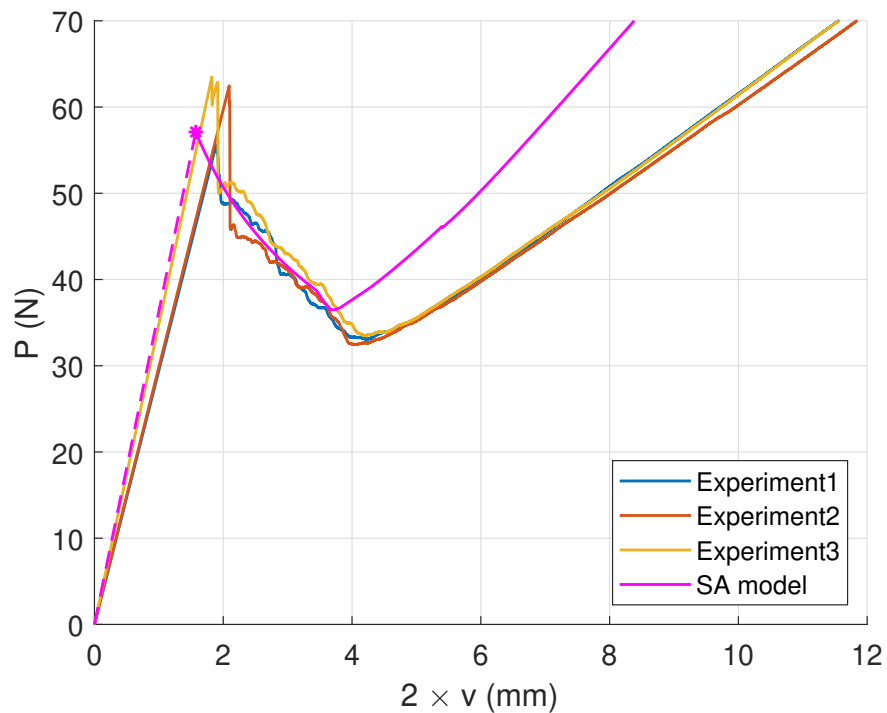


Figure 5.12: Comparison of the SA model against experiments with the fasteners tightened with nominal load

However, there are other factors which could be the culprit for this behaviour. Similar to the DCB specimen with the hole, the crack tip front varies as the hole and the fastener are initiated over the crack growth. This is shown by the FE analysis, but is confirmed by Bastiani[34] as well. Bastiani confirmed in his work that this happens independent of fastener preload. The crack tip front curls around the hole again to form a v-shape front. This is shown in figure 5.13, where the snap through happens between 5.13(b) and (c).

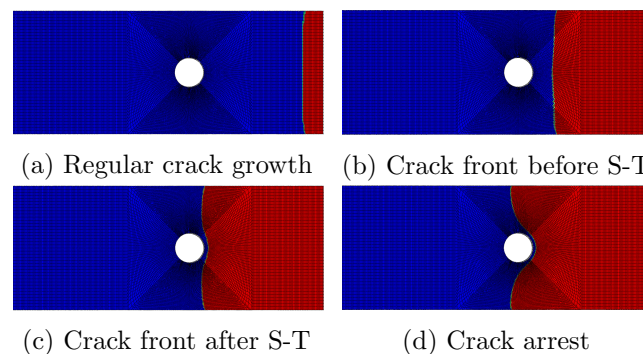


Figure 5.13: Crack tip front of DCB with fastener, the fastener is hidden in the images

In these images the non damaged cohesive is shown in blue again, and the fully damaged and released material is shown in red, and the crack travels from right to left. It is

interesting as the fastener is arresting the snap through behaviour but not preventing it. This arrest of the snap through is also shown in figure 5.14, where the force drop of the FE analysis with the fastener is less severe than the force drop in a DCB specimen with only a hole. After which the two analyses follow their different outcomes of course. Similar to the comparison of the SA model to the preloaded experiments, the initiation of the fastener is earlier in the SA model than the FE analysis. However the deviation in the force increase between the two is less severe than the deviation between the SA model and the experiments. This is because the FE analysis deviates slightly from experimental values, which can be seen in figure 5.15, and in figure 5.10 where the FE curve is on trajectory to cross the experimental curves.

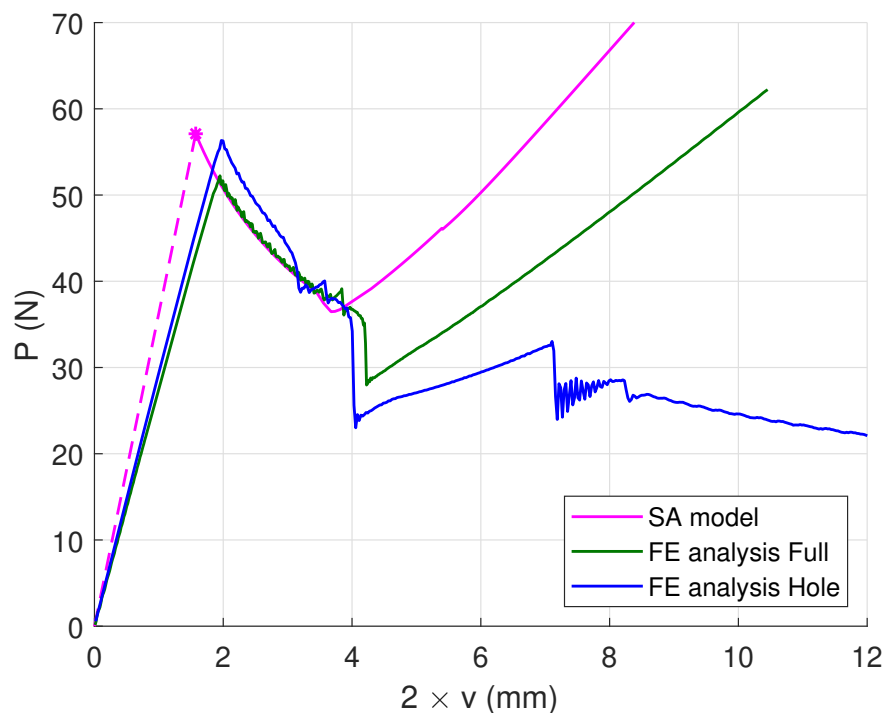


Figure 5.14: Comparison of the SA model against the FE analyses

Figure 5.15 shows that the FE analysis with CZM is a very accurate representation for DCB specimens with fastener without preload. The linear opening is a little too compliant but the propagation curve follows the experimental propagation well. The snap through behaviour is identical and the force increase deviation is minimal.

From the results until now it is clear that the fastener is initiated earlier than the FE analysis or the experiments. However, the question remains how much that influences the SA model on the force increase afterwards. A variable that was looked at to improve the behaviour of the SA model at the crack arrest has been the length of  $s$  when assigning the domains. It was found that the model would decrease in accuracy with increasing the length. This is shown in figure 5.16.

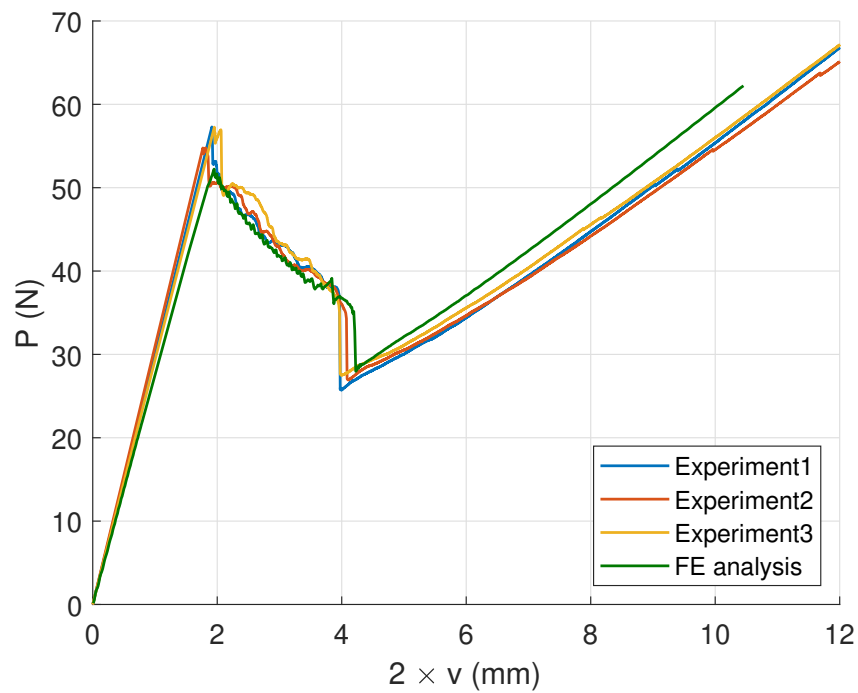


Figure 5.15: Comparison of the FE model against experiments with the fasteners tightened finger tight

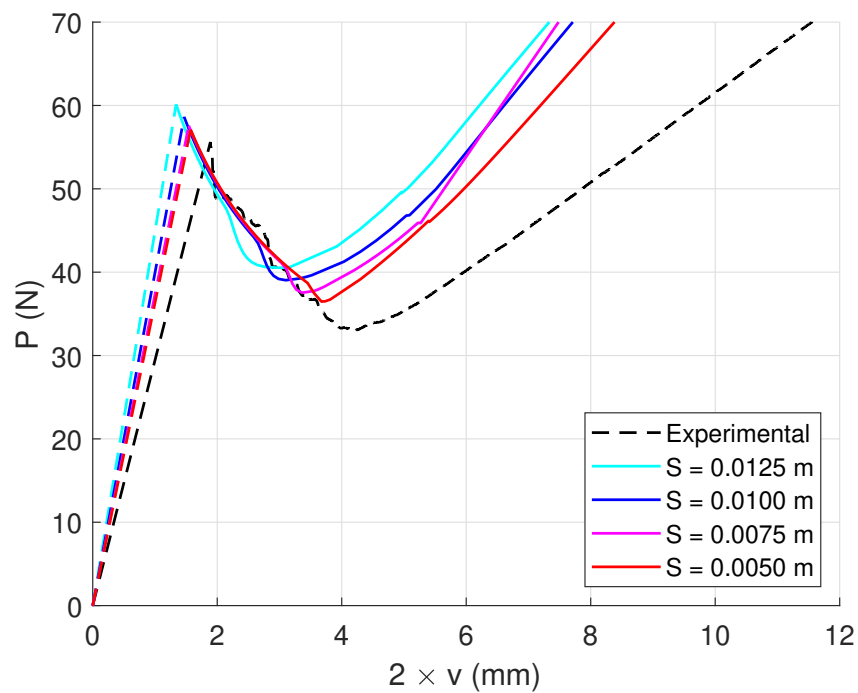


Figure 5.16: The effect of varying length  $s$  ( $m$ ) on the accuracy of the SA model

It can be seen that with a decrease in the size of  $s$ , not only the linear opening would improve compared to experimental values, but also the crack arrest behaviour. This is mostly due to the delay in accounting for the fastener. There is still a variation in the deviation between the crack arrest of the various lengths and the experimental crack arrest. However, this deviation is minimal.

One could argue the best way to improve the SA model is therefore to minimize  $s$  until the SA model is converging with experimental results. This is however impossible with the current set up of the model, as this affects the integration of the different scenarios of the hole in the domains as explained in section 3.7. Due to the current setup of the integrals the minimal length of  $s$  must be at least the diameter of the hole,  $D_H = 4.85 \text{ mm}$ . All results shown previously have been made with  $s = 5 \text{ mm}$ .

Nevertheless, it is no guarantee that the accuracy of the SA model will converge with an ever decreasing  $s$ . As  $s$  will be smaller than  $D_H$ , it is a possibility that the effects of the hole and the fastener will not be captured in full by the middle domain, which will lead to inaccuracies.

Another possibility of inaccuracies is the influence the length of the middle domain has on the approximation curve to the specimen compliance, as discussed in section 3.8. The approximation only uses the middle region to fit a polynomial curve to. So with a smaller region to apply to, it might lose accuracy. Especially as this fitted curve is used by taking its derivative, thus accuracy is required.

Logically the crack arrest of the SA model is depended on the position of the fastener, as a longer arm would have a higher compliance and vice versa. But this is connected to the shape of the crack tip front.

As stated earlier the crack tip front changes its shape around the hole and fastener. As the SA model is a derived from a 2D perspective, this crack tip curvature cannot be replicated. So the model assumes a straight line from the peak of the curvature, but the majority of the crack tip length is larger than assumed at the peak. This leads to reduced bending stiffness and therefore more compliant behaviour.

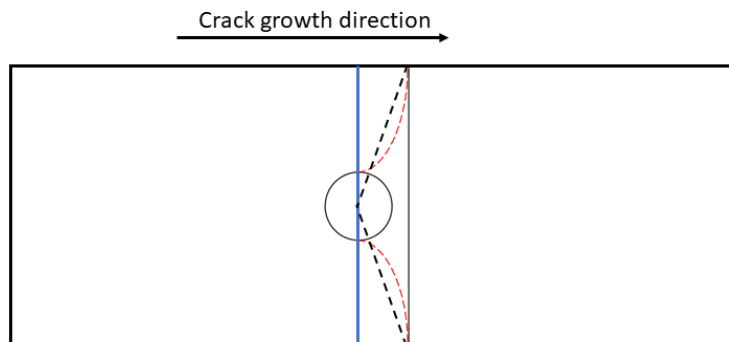


Figure 5.17: Approximation of the crack tip front at crack arrest

However, one aspect of this curvature can be simplified and simulated. The shape of the crack tip leads to less bonding surface in the elastic foundation, as shown in figure 5.17. The crack tip as assumed by the SA model is shown in blue. The curvature, in red,

reduces the bonded area after the crack tip. This can be simplified by drawing two straight lines from the middle of the crack tip to the sides of the specimen, in striped black. This creates two triangles, which reduces the area between the blue and black lines to half its original. Therefore, a simple implementation in the model is to reduce the elastic foundation stiffness to half its original when the crack reaches the hole, to simulate the area reduction by the curvature.

The results of which are shown in figure 5.18. It can be seen that the stiffness of the foundation has no influence on the crack arrest behaviour of the SA model. At the same time, the dependence of the model on the fastener stiffness was also investigated. The SA model reacts by having a small force reduction, however, it is no significant change in the response of the model.

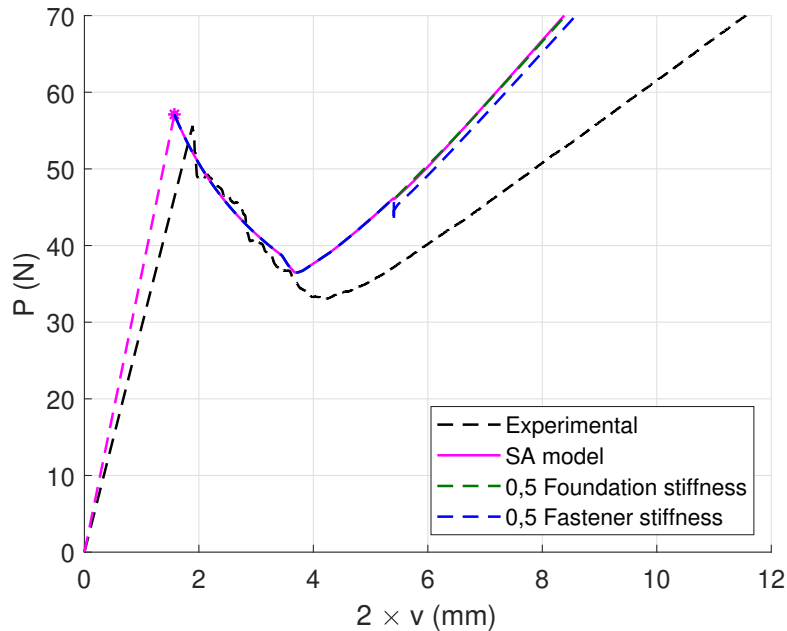
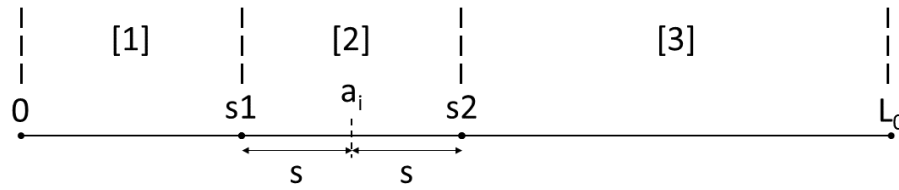


Figure 5.18: Comparison of crack arrest of the regular SA model

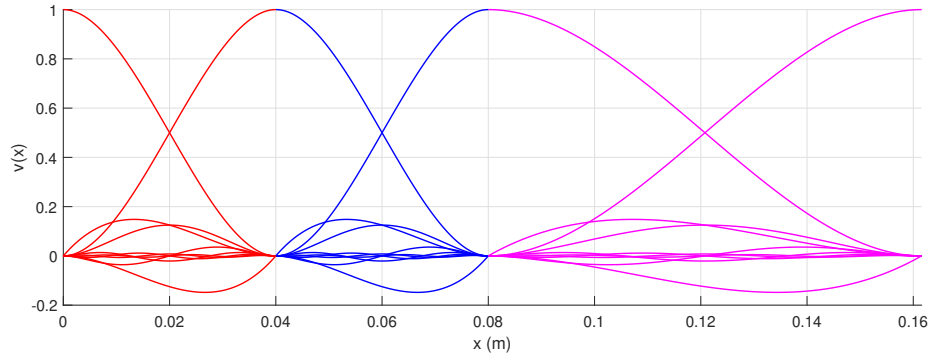
## 5.6 Improvements of the SA model

There were initial possibilities for optimization explored to improve the accuracy of the model. These possibilities were found during development of the model, which are the length of  $s$  for the second domain, and the order of the hierarchical shape functions in each domain. These features are shown again in figure 3.3 below.

As shown before, the length  $s$  does influence the precision of the results of the SA model. However, performance of the SA model is based both on accuracy and run time as the goal of the model is to be a useful design tool to explore specimen parameters before committing to a full computational analysis.



(a) Overview of the domains the specimen is divided into (repeated from page 16)



(b) Example of the sets of shape functions in the domains (repeated from page 16)

Figure 3.3: Overview of the specimen split in domains (repeated from page 16)

First the order of the shape functions were varied. The model would run and the initial critical load and opening would be compared, and the propagation curve, as well as the run time. As domains 1 and 3 have little variation in the displacement field, the order of their shape functions are kept the same and kept low. When the order of the shape functions is given as 4-7-4 e.g., the number correlates to the shape functions in domain 1, 2, or 3 respectively.

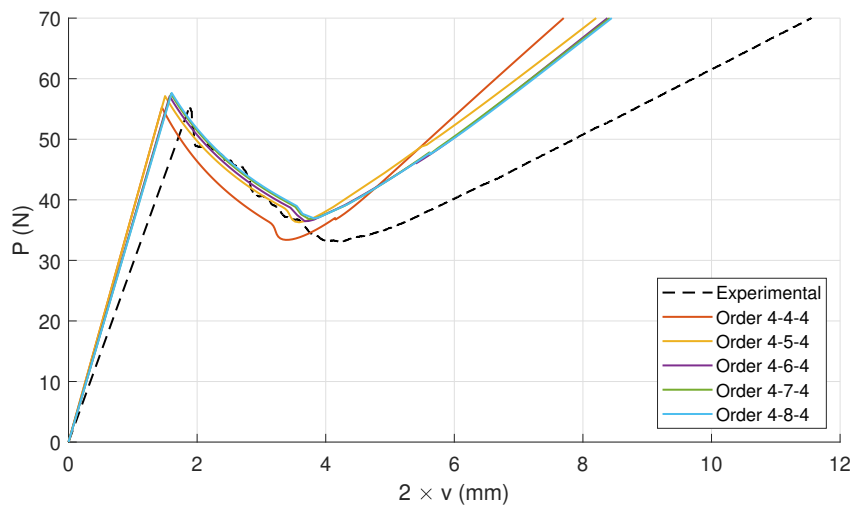
What can be seen in table 5.4 and figure 5.19 is that the SA model converges with increasing order of shape functions. The differences between the initial loads and openings get smaller, the larger the orders become.

Table 5.4: Results or order variation

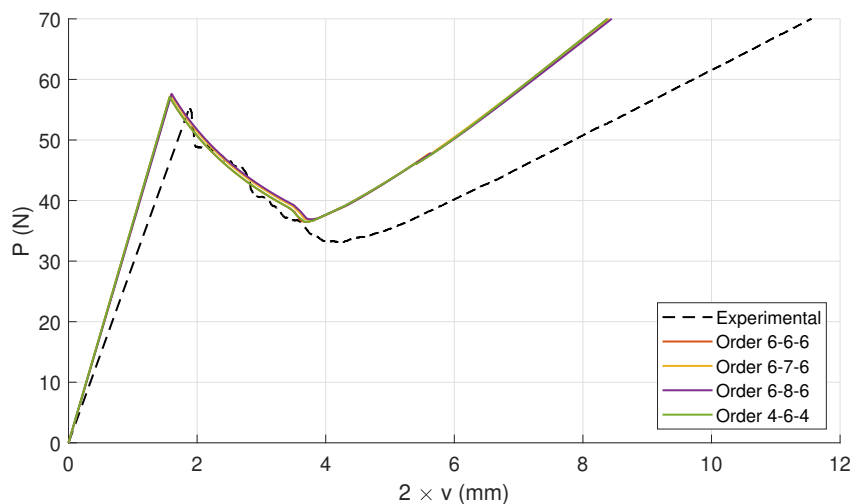
Order	Run time (sec)	$P_c(N)$	$v_c(mm)$
4-4-4	258	55,264	1.452
4-5-4	316	57,130	1.501
4-6-4	407	57,103	1.572
4-7-4	765	57,498	1.593
4-8-4	1492	57,655	1.604
6-6-6	524	57,081	1.571
6-7-6	933	57,474	1.592
6-8-6	1790	57,623	1.603

However it is also visible that there is a minimal order of shape functions needed to provide the precision of the SA model. In figure 5.19a it is clear the 4-4-4 model lacks

accuracy when describing the crack propagation in the DCB specimen. This difference is diminished in the 4-5-4 model, but not completely gone. The differences between the 4-6-4 model and higher order models is negligible. In figure 5.19b it is seen that higher order shape functions in domains one and three do not significantly improve the model's response. Therefore it was chosen to use the 4-6-4 model in all results.



(a) Graphs of different 4-X-4 order models



(b) Graphs of different 6-X-6 order models compared to 4-6-4

Figure 5.19: Graphs of different order models plotted against an experimental curve

Secondly the influence of  $s$  on the SA model response was investigated. As stated, this was done using the 4-6-4 order model. What can be seen in table 5.5 is that the model converges the smaller  $s$  is given as input. What can also be seen in the table is that only positive ratios of  $s/D_H$  were possible. Again, this is due to how the integration of the model is set up. However, to determine if this converges to an infinitesimal small  $s$  or only to a ratio of  $s/D_H = 1$ , a model should be made that could handle  $s/D_H$  ratios

smaller than 1.

Table 5.5: Results of  $s$  variation

$s(mm)$	$s/D_H$	Run time (sec)	$P_c(N)$	$v_c(mm)$
5	1,03	414	57,103	1.572
6	1,24	415	57,190	1.562
7	1,44	402	57,416	1.550
8	1,65	287	57,745	1.532
9	1,86	297	58,153	1.505
10	2,06	340	58,632	1.468
12.5	2,58	349	60,136	1.339
15	3,09	408	62,131	1.189

This convergence is also clear in figure 5.20, but mostly in the crack arrest behaviour. With the exceptions of  $s = 8$  and  $s = 9$  mm, which produced inexplicable errors in the latter stage of crack arrest, all models completed crack arrest. Most interesting is the earlier influence the fastener seems to have with larger  $s$  models. This is most likely due to the fact that within the middle domain, the influence of the fastener can be accounted for more accurately due to the domain size, relative to the other domains, and therefore it is accounted for earlier due to the middle domain being larger.

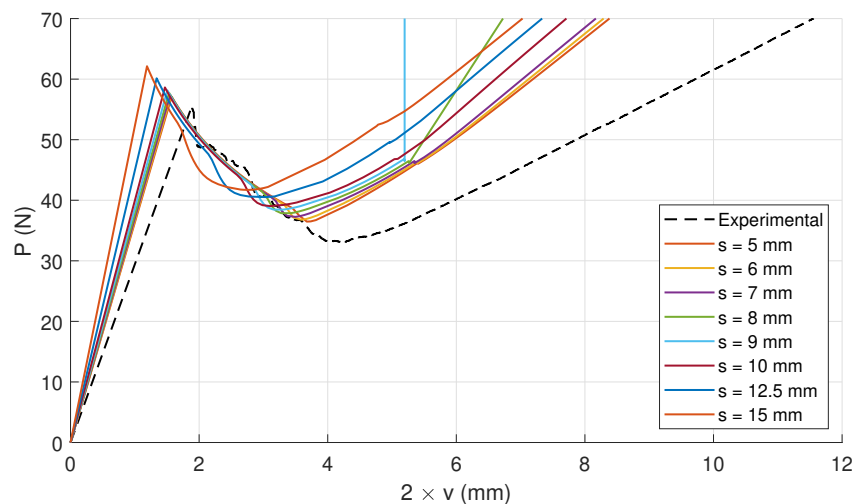


Figure 5.20: The influence of the length  $s$  on the SA model

Another thing that was studied was the influence of both parameters on the run time of the SA model. If the focus is kept on length  $s$ , it can be seen that it had no significant influence on the running time of the SA model, see table 5.5. Again, except for  $s = 8$  and  $s = 9$  mm, which were cut short due to errors, there is no pattern to be seen in the run times of the various models.

This is different when the orders of the shape functions are analysed. In table 5.4 it is not only clear that the run time is increasing with each order increase, but also that the time difference grows each increase of order.

There are two factors at play which both have a large influence the run time of the SA model. First is the moving domain around the crack tip. This not only changes the location of the second domain, but it also changes the ranges of the first and third domain. The effect of that is that the shape functions have to be recalculated, and taken the derivatives from, every time the crack grows for all 3 domains. The result being that adding higher order shape functions to the model, results in more functions needing to be recalculated every time the crack has grown.

This has a secondary result as well. Not only does the moving domain add calculation time in the re-definition of the shape functions, but the changed shape functions also require the integrations of the elastic strains, as shown in section 3.5 to 3.7, to be executed again. This calculation time also increases as higher order shape functions are added.

The second factor is the solving step of the SA model. As shown in section 3.6, the SA model gets rewritten into a system of equations. When higher order functions are added to the model, the size of the system of equations grows and therefore the calculation time to solve increases.

This is exaggerated by the facts that the solving process and the preceding steps have to occur symbolically. In section 3.8 the compliance function of the model needs to be dependent on crack length  $a$ , in order to calculate the SERR with the derivative of the compliance towards  $a$ . To do this,  $a$  is integrated symbolically in the elastic foundation in section 3.7. However, this also leads to the solving of the resulting system of equations needing to be done symbolically. So as the size of the system increases, the time needed to calculate to solution increases even more.

The resulting calculation time is actually still orders smaller than a full FE analysis. The SA model, using 4-6-4 orders and  $s = 5 \text{ mm}$ , provides its solution within 7 minutes for this particular setup of DCB model, compared to approximately 4 hours and 15 minutes for a FE model.

There are of course probabilities to decrease the run time of both models. In the SA model there are improvements thought to be possible in the redefinition of the function domains, the stiffness integrations, and the Newton Raphson iteration scheme. The FE model has possibilities to be optimized for elements size, both at a distance from, and around the hole. The FE model can also be improved by applying a preload to the fastener, though it is unlikely to improve the run time of the model.

Even without these improvements, the SA model still does perform excellently as a design tool, given the relative short run time, in combination with the ease of changing parameters. The SA model can provide comparably accurate results for a range of settings within the time span of one FE analysis.

## Chapter 6

# Conclusions

A novel model to predict and analyse Mode I delamination crack growth in composite structures with fasteners has been presented. The model is based on the Rayleigh Ritz approximation method using Bardell's hierarchical shape functions to represent the displacement field within a DCB specimen. A system of equations was set up using the Principle of Minimal Potential Energy and the hole and the fastener were accounted for in the elastic energy calculation. It has been shown that this method is a viable solution to simulating crack growth in DCB specimens, including fasteners.

The work done in this dissertation is considered a proof of concept for various aspects. Firstly, it has been shown that using the Rayleigh Ritz method is an accurate and effective way to model mode I crack growth in DCB specimens in a simplified 2 dimensional model.

It has also been shown that with the Rayleigh Ritz approximation it is possible to have a division in sub domains of which the boundaries continuously change automatically. The use of sub elements or domains was already proven in multiple literary sources [16, 17, 20, 21], however they worked with non changing element boundaries. Da Silva et al.[18] have shown the method to be accurate with changing sub element lengths, but this was done with separate models instead of being executed with automatically implemented boundary conditions.

Furthermore the implementation of a hole in a DCB specimen has been proven to be possible. The realistic crack growth behaviour of the DCB specimen with a hole has been largely recreated and a very good agreement was found compared to experimental values and a FE analysis using CZM. The limiting factor is found to be the 2D approximation of 3D phenomena happening at the crack tip front, which were found in both the FE analysis and the experiments.

Lastly it has been proven that the implementation of the fastener in a DCB specimen is possible within the Rayleigh Ritz method. The crack growth results were again compared to FEA and experiments, and a good resemblance between them was found. Full crack arrest was realized within the SA model. The differences between the SA model and experimental curves were again thought to be due to 3D shaping of the crack tip front.

A small parameter optimization was executed and correlations were found between accuracy and the length of the middle domain, and between the order of the shape

functions and the accuracy and run time of the model.

There are still possibilities for improvement of the method, which could be of great interest. The exploration of sizes of the middle domain smaller than the fastener diameter is of high interest, to discover if the accuracy is dependent on the absolute size of the middle domain or on the size relative to the fastener. Another area of improvement would be the activation of the fastener if the displacement at the fastener is positive, instead of absolute displacement positive, as the model currently also accounts for fastener compression in the displacement integration, which is unrealistic. Lastly, it would be interesting to see if the 3D phenomena of the crack tip front would be able to replicate in a model which uses 3D panels with a vertical displacement field in both X and Y direction. This would be a completely different set up of the Rayleigh Ritz method and the DCB specimen, and it should be a study on its own.

To conclude, the possibility of modelling crack growth and crack arrest within the Rayleigh Ritz method has been presented in this work. The limitations, the origins thereof, and possible improvements of the model have been discussed. Optimizations in the model were explored and the results have been verified with experimental results and finite element analysis.

# Bibliography

- [1] *AC 20-107B - Composite Aircraft Structure*, 2009. [Online]. Available: Federal Aviation Administration (FAA)
- [2] K. Lin, E. Cheung, W. Liu, and L. Richard, “Delamination/Disbond Arrest Features in Aircraft Composite Structures,” *DOT/FAA/TC-18/5*, p. 131, 2018. [Online]. Available: Federal Aviation Administration (FAA)
- [3] I. Daniel, “Failure mechanisms in fiber-reinforced composites,” 1978.
- [4] W. Liu, “Analysis of Delamination Arrest Fasteners in Bolted-Bonded Composite Structures,” *University of Washington*, p. 46, 2014.
- [5] A. Turon, P. P. Camanho, A. Soto, and E. V. González, “Analysis of delamination damage in composite structures using cohesive elements,” 2018.
- [6] S. Hallett and P. Harper, “Modelling delamination with cohesive interface elements,” in *Numerical modelling of failure in advanced composite materials*. Elsevier, 2015, pp. 55–72.
- [7] L. A. de Oliveira and M. V. Donadon, “Delamination analysis using cohesive zone model: A discussion on traction-separation law and mixed-mode criteria,” *Engineering Fracture Mechanics*, vol. 228, p. 106922, 2020.
- [8] M. V. Donadon and D. P. Lauda, “A damage model for the prediction of static and fatigue-driven delamination in composite laminates,” *Journal of Composite Materials*, vol. 49, no. 16, pp. 1995–2007, 2015.
- [9] R. F. Viana de Melo, “A Numerical Parametric Study on the Effectiveness of Fastener Delamination/Disbond Arrest Mechanism in Composite Laminates under Mode I Loading,” *ITA, São José dos Campos, SP, Brasil*, 2020.
- [10] R. Olsson, “On improper foundation models for the DCB specimen,” in *ICCM International Conferences on Composite Materials*, 2007.
- [11] F. Ozdil and L. Carlsson, “Beam analysis of angle-ply laminate DCB specimens,” *Composites Science and Technology*, vol. 59, no. 2, pp. 305–315, 1999.
- [12] M. Kanninen, “A dynamic analysis of unstable crack propagation and arrest in the DCB test specimen,” *International Journal of Fracture*, vol. 10, no. 3, pp. 415–430, 1974.

- [13] M. Hyer and T. Knott, "Analysis of end-fitting induced strains in axially loaded glass-epoxy cylinders," *Composite Structures for SMES Plants (NISTIR5024)*, (Eds. RP Reed and JD McColskey), Report to Defense Nuclear Agency from Materials Reliability Division, National Institute of Standards and Technology, Boulder, CO, NISTIR, vol. 5024, 1994.
- [14] M. M. Shokrieh and M. Heidari-Rarani, "A comparative study for beams on elastic foundation models to analysis of mode-I delamination in DCB specimens," *Structural Engineering and Mechanics*, vol. 37, no. 2, pp. 149–162, 2011.
- [15] M. Kharazi and H. Ovesy, "Postbuckling behavior of composite plates with through-the-width delaminations," *Thin-Walled Structures*, vol. 46, no. 7-9, pp. 939–946, 2008.
- [16] R. Vescovini and C. Bisagni, "Semi-analytical buckling analysis of omega stiffened panels under multi-axial loads," *Composite Structures*, vol. 120, pp. 285–299, 2015.
- [17] S. G. Castro and M. V. Donadon, "Assembly of semi-analytical models to address linear buckling and vibration of stiffened composite panels with debonding defect," *Composite Structures*, vol. 160, pp. 232–247, 2017.
- [18] D. C. da Silva, M. V. Donadon, and M. A. Arbelo, "A semi-analytical model for shear buckling analysis of stiffened composite panel with debonding defect," *Thin-Walled Structures*, p. 108636, 2021.
- [19] N. Bardell, "Free vibration analysis of a flat plate using the hierarchical finite element method," *Journal of Sound and Vibration*, vol. 151, no. 2, pp. 263–289, Dec. 1991. [Online]. Available: <https://linkinghub.elsevier.com/retrieve/pii/0022460X9190855E>
- [20] S. G. Castro, T. A. Guimarães, D. A. Rade, and M. V. Donadon, "Flutter of stiffened composite panels considering the stiffener's base as a structural element," *Composite Structures*, vol. 140, pp. 36–43, 2016.
- [21] O. D. de Matos Junior, M. V. Donadon, and S. G. Castro, "Aeroelastic behavior of stiffened composite laminated panel with embedded SMA wire using the hierarchical Rayleigh–Ritz method," *Composite Structures*, vol. 181, pp. 26–45, 2017.
- [22] E. S. Greenhalgh, "4 - Delamination-dominated failures in polymer composites," in *Failure Analysis and Fractography of Polymer Composites*, ser. Woodhead Publishing Series in Composites Science and Engineering. Woodhead Publishing, 2009, pp. 164–237. [Online]. Available: <https://www.sciencedirect.com/science/article/pii/B9781845692179500044>
- [23] A. A. Griffith, "VI. The phenomena of rupture and flow in solids," *Philosophical transactions of the royal society of london. Series A, containing papers of a mathematical or physical character*, vol. 221, no. 582-593, pp. 163–198, 1921.
- [24] G. Irwin, "Fracture. Encyclopaedia of Physics, Vol. VI," *Springer-Verlag*, vol. 1, no. 168, p. 9, 1958.

- [25] R. Krueger, “The virtual crack closure technique for modeling interlaminar failure and delamination in advanced composite materials,” in *Numerical modelling of failure in advanced composite materials*. Elsevier, 2015, pp. 3–53.
- [26] J. R. Reeder, “A bilinear failure criterion for mixed-mode delamination,” in *Eleventh Volume: Composite Materials—Testing and Design*. ASTM International, 1993.
- [27] M. L. Benzeggagh and M. Kenane, “Measurement of mixed-mode delamination fracture toughness of unidirectional glass/epoxy composites with mixed-mode bending apparatus,” *Composites science and technology*, vol. 56, no. 4, pp. 439–449, 1996.
- [28] D. Dugdale, “Yielding of steel sheets containing slits,” *Journal of the Mechanics and Physics of Solids*, vol. 8, no. 2, pp. 100–104, 1960. [Online]. Available: <https://www.sciencedirect.com/science/article/pii/0022509660900132>
- [29] G. I. Barenblatt, “The mathematical theory of equilibrium cracks in brittle fracture,” in *Advances in applied mechanics*. Elsevier, 1962, vol. 7, pp. 55–129.
- [30] W. Ritz, “Über eine neue methode zur lösung gewisser variationsprobleme der mathematischen physik.” 1909.
- [31] R. Olinde, “De l’attraction des spheroides,” *Correspondence sur l’École Imperiale Polytechnique*, vol. 3, no. 3, pp. 361–385, 1816.
- [32] R. Olsson, “A simplified improved beam analysis of the DCB specimen,” *Composites Science and Technology*, vol. 43, no. 4, pp. 329–338, 1992.
- [33] K. Kondo, “Analysis of double cantilever beam specimen,” *Advanced Composite Materials*, vol. 4, no. 4, pp. 355–366, 1995.
- [34] G. Bastiani, “Experimental Study of Fasteners as a Delamination Arrest Mechanism in Composite Laminates under Mode I Loading,” *ITA, São José dos Campos, SP, Brasil*, 2021.
- [35] B. Endo, “Caracterização da tenacidade à fratura interlaminar de um material compósito de fibra de carbono-epoxi considerando influência termomecânica,” *ITA, São José dos Campos, SP, Brasil*, 2014.
- [36] LISI Aerospace, “HI-LITE ST collar,” *Lisi Aerospace*, pp. 1–2, 1985.
- [37] —, “HI-LITE PIN TITANIUM HST10,” *Lisi Aerospace*, vol. 1, no. 1, pp. 1–2, 1982.
- [38] ASTM International, “Standard Test Method for Mode I Interlaminar Fracture Toughness of Unidirectional Fiber-Reinforced Polymer Matrix Composites,” American Society for Testing and Materials, West Conshohocken, PA, USA, Standard ASTM D5528-13;2018, 2018. [Online]. Available: <https://www.astm.org/Standards/D5528.htm>

## Appendix A

# Filtering of FE data

This appendix purpose is to show the difference between the raw and filtered data from the FE model using a decimation filter. The differences are relatively small, however the filtered data gave a better interpretation of the processes around the hole and the fastener when they were implemented. A decimation factor of 15 was used for the decimation filter.

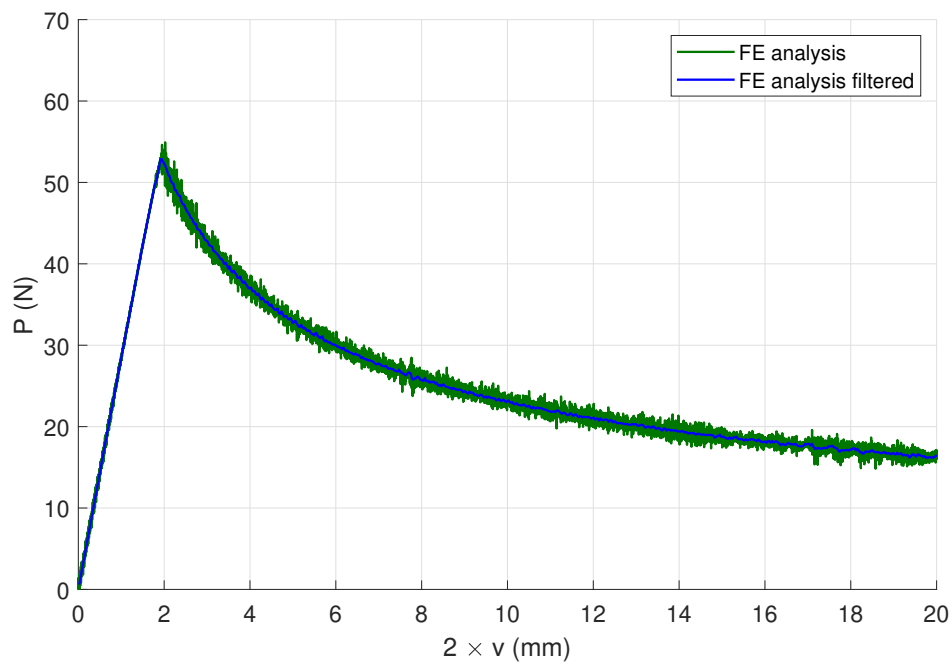


Figure A.1: Raw vs. filtered data of the Plain DCB FE model

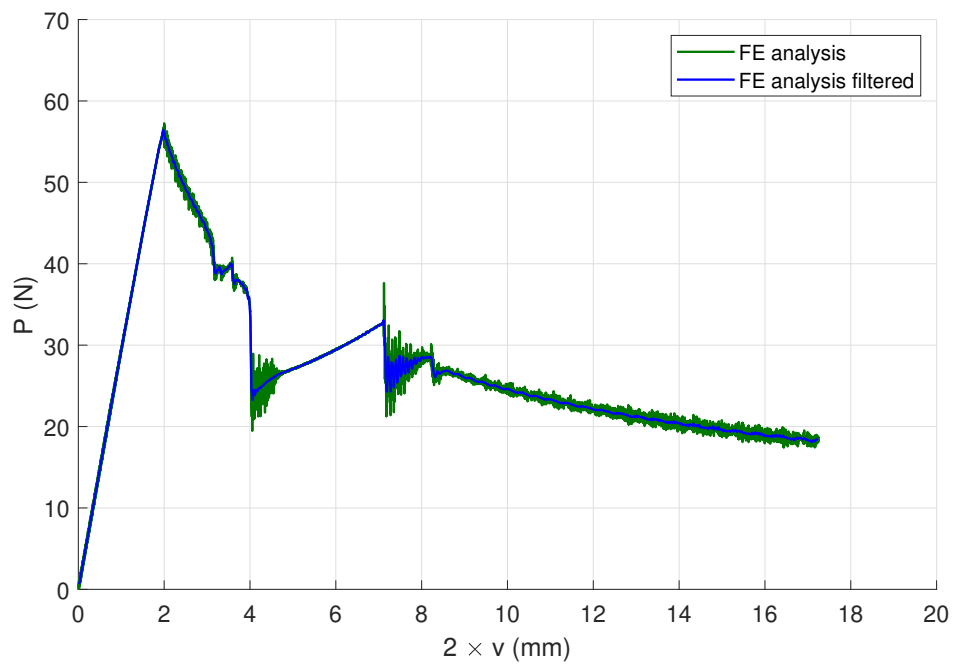


Figure A.2: Raw vs. filtered data of the DCB specimen with hole FE model

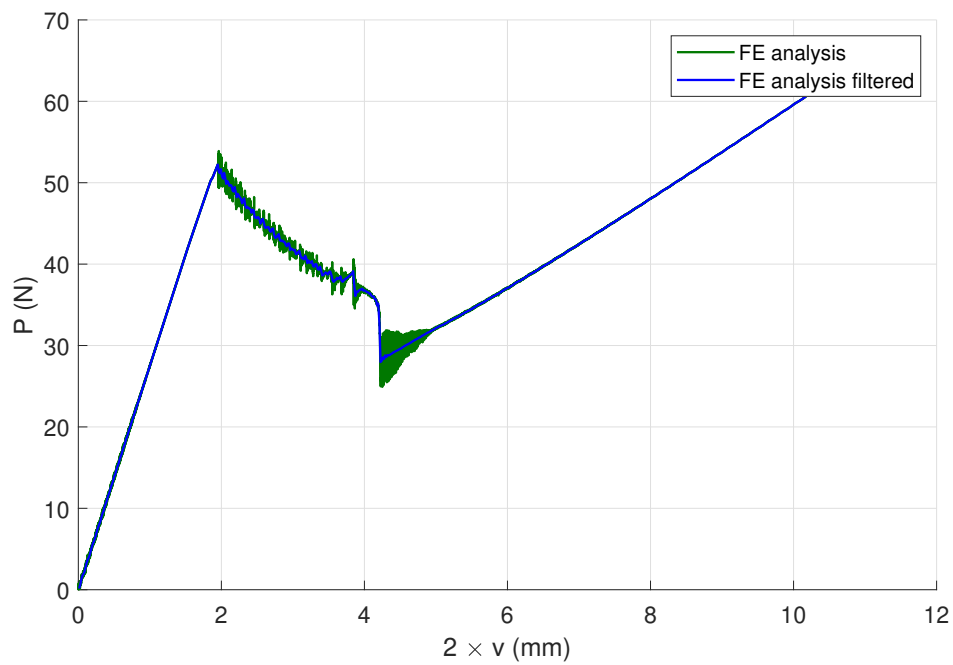


Figure A.3: Raw vs. filtered data of the DCB specimen with hole and fastener FE model